Figure: Filtered aeromagnetic data (Fig. A) reveal buried seismogenic faults along the actively-deforming hinge zone of Malawi Rift's North Basin. Further enhancement of the data (Fig. A inset) shows that pre-existing basement fabric aligns with the segments of the buried active faults (Fig. B).

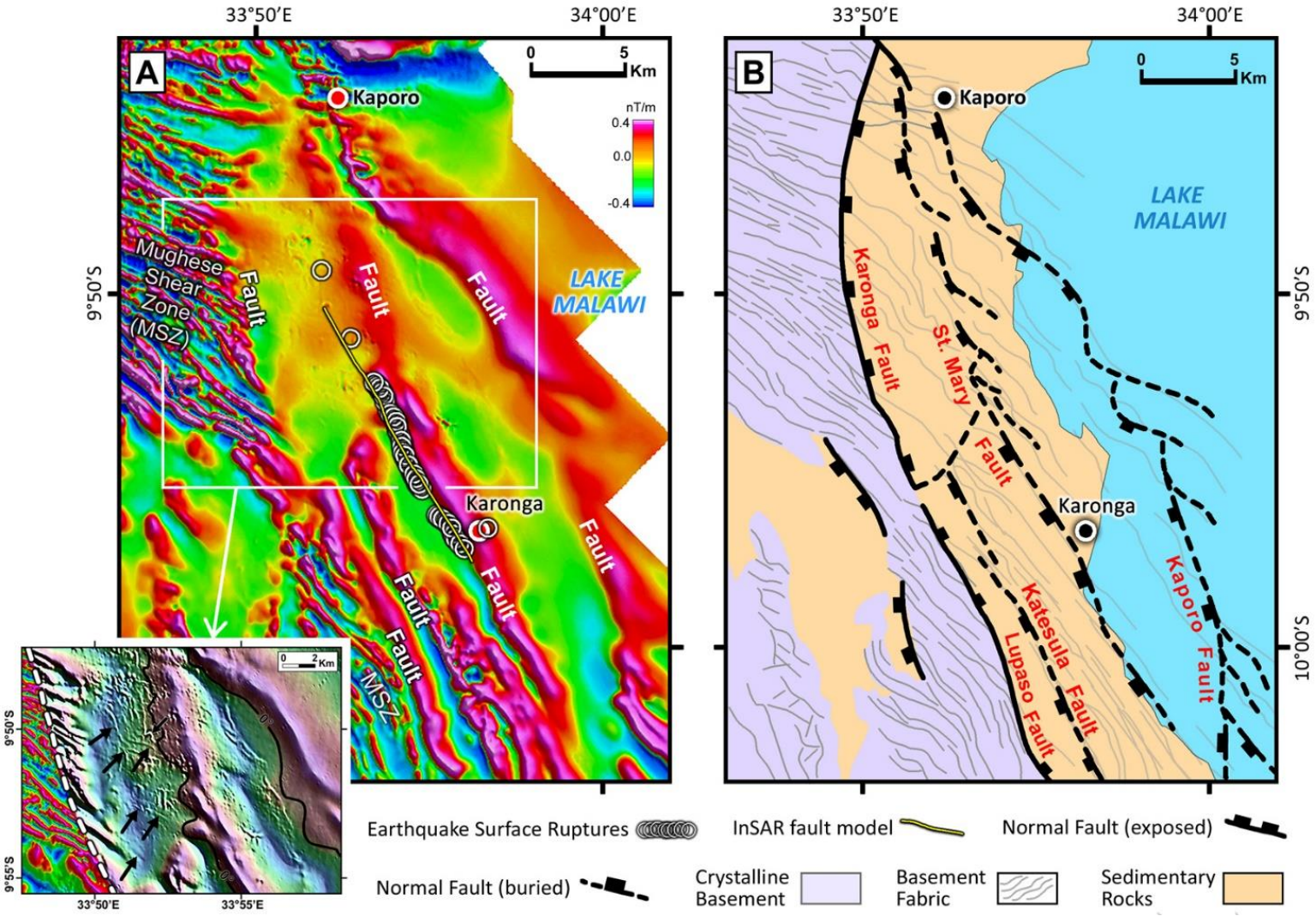

Active deformation of Malawi Rift's North Basin hinge zone modulated by reactivation of pre-existing Precambrian shear zone fabric

F. Kolawole[1*], E. A. Atekwana[1**], D. A. Laó-Dávila[1], M. G. Abdelsalam[1], P. R. Chindandali[2], J. Salima[2], and L. Kalindekafe[3]

[1]Oklahoma State University Main Campus, Stillwater, OK 74078, United States

[2]Geological Survey Department of Malawi, P.O. Box 27, Zomba, Malawi

[3]Malawi University of Science and Technology, P.O. Box 5196, Limbe, Malawi

*now at the ConocoPhillips School of Geology and Geophysics, University of Oklahoma, Norman, OK, United States

**now at the College of Earth, Ocean, and Environment, University of Delaware, Newark, DE, United States

Corresponding author: Estella Atekwana (estella.atekwana@okstate.edu)

Key Points:

1. Aeromagnetic data elucidates the relationship between the 2009 Mw 6.0 Karonga, Malawi earthquake surface ruptures and buried faults.
2. Surface rupture locations align with a distinct magnetic lineament in the basement.
3. Strain accommodation in the North Basin hinge zone is modulated by reactivation of the underlying Precambrian shear zone fabric.

Abstract

We integrated temporal aeromagnetic data and recent earthquake data to address the long-standing question on the role of pre-existing Precambrian structures in modulating strain accommodation and subsequent ruptures leading to seismic events within the East African Rift System (EARS). We used aeromagnetic data to elucidate the relationship between the locations of the 2009 M_w 6.0 Karonga, Malawi earthquake surface ruptures and buried basement faults along the hinge zone of the half-graben comprising the North Basin of the Malawi Rift. Through the application of derivative filters and depth-to-magnetic-source modeling, we identified and constrained the trend of the Precambrian metamorphic fabrics and correlated them to the three-dimensional (3D) structure of buried basement faults. Our results reveal an unprecedented detail of the basement fabric dominated by high frequency WNW- to NW-trending magnetic lineaments associated with the Precambrian Mughese Shear Zone fabric. The high frequency magnetic lineaments are superimposed by lower frequency NNW-trending magnetic lineaments associated with possible Cenozoic faults. Surface ruptures associated with the 2009 M_w 6.0 Karonga earthquake swarm aligned with one of the NNW-trending magnetic lineaments defining a normal fault that is characterized by right-stepping segments along its northern half and coalesced segments on its southern half. Fault geometries, regional kinematics and spatial distribution of seismicity suggest that seismogenic faults reactivated the basement fabric found along the half-graben hinge zone. We suggest that focusing of strain accommodation and seismicity along the half-graben hinge zone is facilitated and modulated by the presence of the basement fabric.

Keywords: Malawi Rift, North Basin, Karonga Basin, 2009 Karonga Earthquake, Shear zone, Reactivation, Pre-existing structures, Normal fault

1. Introduction

The contributions of faulting and magmatism to strain accommodation within weakly extended, magma-poor youthful continental rifts remain poorly-understood as there are limited locations worldwide where these processes can be actively documented. The East African Rift System (EARS; Figure 1a) is the largest seismically-active rift system on Earth in which deep seismicity is localized along or near major border faults, while relatively shallower seismicity is mostly associated with strain localization within the rift axis [*Kearey et al*., 2009; *Craig et al*., 2011]. Absence of basin-ward migration of faulting and an overall extension localization on faults established in the early stage of rifting has been observed in a part of the EARS [*McCartney and Scholz*, 2016]. However, numerous studies have shown that extension in the early stage of rifting is accommodated by displacement along border faults. As rifts evolve, extension is transferred to the hanging-wall, often facilitated by diking and magma intrusion [e.g. *Ebinger and Casey*, 2001; *Goldsworthy and Jackson*, 2001; *Wright et al*., 2006; *Calais et al.*, 2008]. It has been shown that the localization of brittle deformation within the border fault hanging-wall is not entirely controlled by the flexure of the hanging-wall, but can be assisted by intrusion and release of magmatic volatiles into the hanging-wall [*Muirhead et al*., 2016]. Located within the southern segment of the EARS, the North Basin of the Malawi Rift (Figure 1b) is a rift in which basin-ward migration of tectonic activity has been proposed [*Biggs et al.*, 2010].

On a continental scale, studies have documented the influence of pre-existing structures associated with Precambrian orogenic belts in facilitating localization of extension during the initiation of rifting in different segments of the EARS [*Versfelt and Rosendahl*, 1989; *Wheeler and Karson*, 1989; *Ring*, 1994; *Modisi et al*., 2000; *Kinabo et al*., 2007; 2008; *Katumwehe et al.*, 2015; *Leseane et al.*, 2015]. On a basin scale, studies have also highlighted the role of pre-existing

structures in determining the compartmentalization and internal structural architecture of individual rift basins [e.g., *Mortimer et al.*, 2016a; *Phillips et al*., 2016]. Most studies that investigated the influence of pre-existing metamorphic basement structures (here referred to as basement fabric) on rift development relied on kinematic analysis of geologic field data [e.g. *Ring*, 1994; *Beacom et al.*, 2001; *Ring et al.*, 2005], interpretation of remote sensing data [e.g., *Laó-Dávila et al*., 2015], interpretation of two-dimensional (2-D) crustal-scale active-source seismic data [e.g. *Wilson et al.*, 2010], three-dimensional (3-D) active-source seismic data [e.g. *Phillips et al*., 2016], fault plane solutions from passive seismic data [e.g. *Hussein et al.*, 2006], and numerical and analogue modeling [e.g., *Morley et al*., 2004; *Corti et al.*, 2007]. While these approaches produced significant results, recent work also highlighted the importance of high resolution aeromagnetic data in understanding the complexity of the influence of basement fabric in the evolution of continental rifts including their nucleation, segmentation, and termination [e.g., *Katumwehe et al*., 2015]. Further, the role of basement fabric in modulating intraplate seismicity has been observed in segments of the Precambrian structures in eastern Africa. For example, earthquakes in South Sudan have been associated with reactivation of the Precambrian Aswa Shear Zone [Figure 1a; *Moussa, 2008*]. Nonetheless, the continual role of basement fabric in shaping the architecture of rift systems and subsequent ruptures leading to seismic events has not been fully understood.

The EARS, especially its Western Branch, is predominantly made-up of half-graben basins linked by step-over transfer zones [e.g., *Rosendahl*, 1987; *Chorowicz*, 2005]. The half-grabens are typically 20-50 km wide with hanging-wall blocks deformed by normal faults that are both synthetic and antithetic to a single master border fault [e.g., *Rosendahl et al.*, 1986; *Rosendahl*, 1987; *Bott*, 1997]. The architecture of a half-graben typically consists of a border fault zone, the

hanging-wall zone and the hinge zone [Figures 1c and d; e.g., *Rosendahl et al.*, 1986; *Morley*, 1995; *McCartney and Scholz*, 2016]. The border fault zone refers to the region around the deepest side of the half-graben, where depocenters containing up to several kilometers of sediment thickness lie adjacent to the master border fault [e.g., *Wheeler and Karson*, 1989; *Withjack et al.*, 2002]. The hanging-wall zone represents the rift floor which lies between the border fault zone and the hinge zone. The hinge zone is the area of greatest curvature in the hanging-wall, which is commonly assumed to have developed passively as a result of crustal flexure in response to vertical displacements along the master border fault.

In this study, we show that the distribution of brittle strain along the hinge zones of weakly extended magma-poor half grabens is not entirely caused by crustal flexure, but can be facilitated and modulated by basement fabric. The recent 2009 Karonga earthquake swarm and the 2014 Karonga earthquake sequence in northern Malawi Rift, a sign of active deformation, were localized along the hinge zone of the half-graben comprising the North Basin of the Malawi Rift (here referred to as half-graben hinge zone) [Figures 1b and 2; *Biggs et al*., 2010; *Oliva et al.*, 2016]. These seismic events allow us to address the persistent question of whether and how basement fabric modulate strain accommodation and seismicity in weakly extended, magma-poor continental rifts, particularly in areas where it has been proposed that reactivation of older structures is not occurring [*Fagereng*, 2013]. Although there is lack of subsurface data (e.g. in the form of seismic data; Figure 2 Inset) along the on-shore part of the half-graben hinge zone, however, the availability of temporal aeromagnetic data and their effectiveness in imaging basement fabric and basement faults provide an unprecedented view of the geological architecture of the half-graben hinge zone and corroborates previous seismic interpretation of faults along the hinge zone (Figure 3).

We use derivative filters to enhance the magnetic anomalies of the basement fabric and faults which revealed the detailed geometry of the Precambrian Mughese Shear Zone (MSZ) and younger faults, possibly Cenozoic in age. We determine the spatial correlation between basement fabric, basement faults and the locations of the 2009 Karonga earthquake surface ruptures in order to assess the role of basement fabric in facilitating fault ruptures that trigger moderate magnitude earthquakes. Here, we show that the deformation of the half-graben hinge zone is actively modulated by reactivation of the basement fabric.

2. Recent Earthquakes in Northern Malawi Rift

2.1. The 2009 Karonga Earthquake Swarm

The Karonga area, located in the North Basin of the Malawi Rift was affected by multiple episodes of M_w 4.9 – 6.0 earthquakes between December 6 and 19, 2009 (Figure 2). The series of earthquakes damaged thousands of houses and resulted in several fatalities [*Biggs et al*., 2010]. Additional series of $M_b \leq 4.6$ earthquakes were recorded until one month after the larger events [*Hamiel et al*., 2012]. The $M_w \geq 4.9$ earthquakes, occurring at <10 km focal depths, were accompanied by coseismic surface ruptures of 35 - 43 cm vertical displacements [*Hamiel et al*., 2012; *Macheyeki et al.,* 2015] and liquefaction-related sand blows within the surficial coastal plain sediments. Differential Interferometric Synthetic Aperture Radar (DInSAR) modeling of the surface deformation associated with the coseismic events suggest that the earthquakes were not associated with magmatic emplacement [*Biggs et al*., 2010]. Instead, these studies found that the earthquake sequence was associated with the rupture of a shallow single NNW-SSE striking and SW-dipping normal fault [*Biggs et al.*, 2010; *Hamiel et al*., 2012; *Macheyeki et al.*, 2015]

associated with active deformation of the half-graben hinge zone. *Hamiel et al.* [2012] documented a cumulative surface rupture length of 18 km, while *Macheyeki et al*. [2015] estimated a total rupture length of 14.3 km. *Macheyeki et al.* [2015] suggested that the fault that ruptured during the earthquake has three segments with observed ~1.6 km-long along-strike separation between them. Since the ruptured fault had no known surface expression before the earthquake swarm, its origin is unknown. It is also not clear if the rupture created a new fault or occurred on a pre-existing fault.

2.2. The 2014 Karonga Earthquake Sequence

Between December 31, 2014 and January 1, 2015, three M_w 5.1 seismic events were recorded by the SEGMeNT (Study of Extension and maGmatism in Malawi aNd Tanzania) array [*Oliva et al.,* 2016]. The earthquake epicenters were located within the Mwenitete-Kaporo area (~15 km north of Karonga town), with hypocentral locations at 5-10 km depths. The fault plane solutions for the earthquake sequence suggest normal faulting on N-S and NNW –striking planes.

3. Geological and Tectonic Setting

3.1. The Malawi Rift

The magma-poor Malawi Rift can be divided into three segments [Figure 1b; *Carter and Bennett*, 1973; *Ebinger et al.,* 1989; *Ring,* 1994; *Laó-Dávila et al.,* 2015]: (1) The northern segment that consists of the North Basin (also known as the Karonga Basin), the Usisya Basin, Mbamba Basin and the Bandwe Basin. The North Basin has a SW-dipping border fault and the basin is tilted to the northeast. The Usisya Basin has an E-dipping border fault and the basin tilts to the west. The

Mbamba Basin has a W-dipping border fault and the basin tilts to the east, and the Bandwe Basin has an E-dipping border fault while the basin tilts to the west. (2) The central segment consisting of the Metangula and Mtakataka Basins have poorly-developed border faults that are mostly W-dipping faults. Both basins are tilted to the east. (3) The southern segment of the rift consists of a bifurcated and southward-shallowing graben system that terminates at the WNW-ESE -trending Shire Graben.

3.2. The North Basin

The North Basin is a typical half-graben, bound on the east by the 100 km-long, NW- striking and steeply (60°) SW-dipping Livingstone border fault [*Wheeler and Karson*, 1989; *Mortimer et al.*, 2016b; Figures 2 and 3a]. The hanging-wall block of the fault has been deformed by numerous NW-striking ~55° west-dipping intra-basin normal faults found under Lake Malawi [Figure 3a; *Mortimer et al*., 2007]. Most of these intra-basin normal faults are synthetic to the Livingstone Fault [*Ring*, 1994; *Mortimer et al*., 2007]. The North Basin is filled with Neogene-Quaternary Chiwondo and Chitimwe lacustrine sedimentary rocks, which in turn are covered by coastal plain alluvial sediments [*Schrenk et al*., 1993; *Ring*, 1994]. The Quaternary alluvial sediments are composed of sandy clays, terrace sands and gravels [*Macheyeki et al*., 2015].

The kinematic history of the North Basin has been attributed to an initial ENE-WSW directed orthogonal extension during which the development and segmentation of the Livingstone border fault occurred, as well as the development of NW-trending hanging wall normal faults (Figures 1c and d) within the basin [*Ring*, 1994; *Mortimer et al*., 2007]. At 500-400 Ka, tectonic extension rotated into a WNW-ESE direction, such that former intra-basin dip-slip faults were

reactivated as oblique dextral strike-slip faults and associated flower structures [*Ring*, 1994; *Mortimer et al*., 2007]. The Livingstone Fault, which borders the North Basin in the east (Figures 2 and 3a), originated as a reactivation of Precambrian ductile shear zones within the Ubendian Belt, and has accommodated at least 4 km of vertical displacement [*Wheeler and Karson*, 1989]. On the half-graben hinge zone, the Precambrian rocks of the MSZ are truncated by the N-S - trending and E-dipping Karonga Fault, juxtaposing the Precambrian rocks against the Mesozoic and Cenozoic sedimentary rocks of the basin. The Karonga Fault, which is one of the most dominant morpho-structural features on the half-graben hinge zone [*Laó-Dávila et al*., 2015] outcrops of Late Carboniferous - Early Jurassic sedimentary rocks, suggesting that the fault predates Cenozoic rifting in northern Malawi. Using Global Positioning System (GPS), earthquake slip vectors and a rigid plate model, *Stamps et al.* [2008] estimated a rift opening rate of 3.8 mm/year, while *Saria et al.* [2014] estimated 2.2 mm/year, and an E-W present-day tectonic extension direction for the North Basin of the Malawi Rift.

3.3. Pre-Malawi Rift Formations

The North Basin is underlain by Paleoproterozoic amphibolite, grey gneisses and granites formed during the Ubendian Orogeny (1,600 Ma) [*Ring et al*., 2002], which were later deformed by the ~30-50 km-wide NW-trending Mughese Shear Zone (MSZ) in the Neoproterozoic (Figure 3a). The Ubendian orogenic belt is composed of different accretionary terranes bounded by steep shear zones [*Delvaux et al*., 2012], among which the MSZ forms the boundary between the Mbozi Terrane to the north and the Ufipa Terrane to the south [Daly, 1988]. The shear zone developed during the Neoproterozoic - Early Paleozoic Pan African Orogeny (550±100 Ma) in which crustal

shortening along the southern boundary of the Ubendian Belt produced sub-vertical sinistral shear zones with the formation of well-developed fabric that were distributed throughout the crust [*Ring et al.*, 2002]. The shear zone is characterized by steeply-dipping (60°-85°) mylonitic fabric [*Ring*, 1994; Figures 3b and c; Figure 3c inset] that contains prominent stretching lineation. The shear zone is also characterized by the presence of shear zone-parallel isoclinal intrafolial folds overprinting earlier structures in the Paleoproterozoic rocks [*Ring*, 1993; *Ring et al.*, 2002].

Patches of Permo-Triassic (Karoo) sedimentary rocks crop out onshore along the Karonga Fault in the western part of the half-graben hinge zone (Figure 3a). The Karoo sedimentary rocks are composed of volcano-sedimentary successions deposited within NE- to NNE and N-trending grabens, and these are intruded by NE-striking doleritic dikes. The regional extension direction during the Karoo is controversial. Based on the fault trends within the Zambezi Rift (south of Malawi Rift), an ENE-WSW directed extension has been inferred [*Daly et al*., 1989]; while a NW-SE directed extension due to the dominant NE to NNE strike of the Karoo rifts and associated doleritic dikes has also been suggested [*Castaing*, 1991]. In the Early Cretaceous, NE-directed extension in the North Basin area resulted in the deposition of fossiliferous red, fluviatile sandstone and siltstones referred to as the 'Dinosaur Beds' [*Jacobs et al*., 1990; *Ring*, 1994].

4. Data and Methods

In this study, we analyzed pre- and post-earthquake aeromagnetic data, spatial location of surface ruptures and sand blows (both here referred to as surface ruptures), and earthquake epicenter locations. A total of 396 surface rupture location coordinates [*Macheyeki et al*., 2015] and eight (8) surface rupture locations [*Hamiel et al*. [2012] along with 229 epicenter location coordinates

of earthquakes associated with the 2009 Karonga earthquake swarm [*Seismological Bulletin of Malawi*, 2015] were used in this study.

4.1. Aeromagnetic data

The pre-earthquake aeromagnetic data covering the half-graben hinge zone used in this study was acquired in 1984-1985, with 120 m flight elevation along NE–SW lines with spacing of 1 km and a tie-line spacing of 10 km. The post-earthquake aeromagnetic data used in this study was acquired in 2013 with a flight elevation of 80 m along NE–SW lines with spacing of 250 m. The tie lines were oriented NW–SE and spaced 5 km apart. The pre- and post- earthquake residual magnetic field data were first reduced to the magnetic pole (RTP) [*Baranov*, 1957; *Arkani-Hamed*, 1988] in order to remove the skewness of the anomalies and correctly position magnetic anomalies directly over their sources, thereby making it possible to correlate the anomalies with geological information. To compare the pre- and post-earthquake aeromagnetic maps, we upward-continued the 2013 map to 120 m (flight elevation of the 1984-1985 map), however, due to the difference in line spacing, the 2013 data has a higher resolution (62.5 m) than the 1984-1985 data (250 m). Edge-enhancement directional filters such as the horizontal gradient magnitude (HG), vertical (Dz) and tilt-angle derivative filters were applied to the RTP aeromagnetic grids in order to enhance shallow subsurface anomalies and highlight structural features [*Ma et al*., 2012]. In order to better delineate faults that have surficial expression in the study area, we draped the filtered aeromagnetic maps on hillshade topographic map of 90 m spatial resolution Shuttle Radar Topography (SRTM) Digital Elevation Model (DEM) (Figure 4). Since there is no report of volcanic sediments or information on remanent magnetization along the half-graben hinge zone, we assume that

magnetization within the study area is largely by induction and that the crystalline basement is the dominant magnetic source.

According to *Miller and Singh* [1994] and *Salem et al.* [2007], the first order vertical derivative, first order horizontal gradient and tilt-angle derivative of the RTP aeromagnetic grid enhance the magnetic signatures of shallow crustal structures. The vertical derivative (Dz) estimates the rate of change of total magnetic intensity in the vertical direction. Total horizontal derivative (horizontal gradient magnitude) estimates the rate of change of total magnetic intensity in the horizontal-X and horizontal-Y directions. The horizontal-X derivative (Dx) operator estimates the rate of change of total magnetic intensity in the E-W direction, thus enhancing structures that are oriented N-S or sub-parallel to the N-S. The horizontal-Y derivative (Dy) operator estimates the rate of change of total magnetic intensity in the N-S direction, thus enhancing structures that are oriented E-W or sub-parallel to the E-W. The tilt-angle derivative is essentially a ratio of the vertical derivative to the total horizontal derivative, thus estimating the magnitude of the overall rate of change of total magnetic intensity (in all directions). The tilt-angle derivative is one of the most effective edge-detection filters because it normalizes all the edges in a dataset, such that edges that are subtle and less evident in the horizontal and vertical derivative maps are well enhanced in the tilt-angle derivative map. Since magnetic lineaments representing faults are well imaged on vertical [*Kinabo et al.*, 2007; 2008] and tilt-angle derivative maps, we delineate the variations in the along-strike and across-strike geometry of magnetic lineaments that represent faults by applying Dx and Dy directional filters to the vertical and tilt-angle derivative maps depending on the orientation of the target faults [*Cooper and Cowan*, 2006]. Furthermore, we enhanced the subtle normalized lineaments observed in the tilt-angle derivative map (low

amplitude, high frequency and short wavelength gradients) by applying 45º directional gradient to the tilt-angle derivative grid.

Grauch and Hudson [2007; 2011] presented simple models describing the various magnetic expressions of normal faults that juxtapose bodies of contrasting magnetic susceptibilities against one another. In this paper, we interpret basement-rooted normal faults along the half-graben hinge zone in terms of the *Grauch and Hudson* [2007; 2011] thin-thick layers variation-2 model, which shows that a normal fault juxtaposing a highly-magnetized basement against an overlying material of lower magnetic susceptibility is characterized by a magnetic-high anomaly above the footwall and a magnetic-low above the hanging wall. Although it is difficult to determine the sense of displacement and amount of fault throw from aeromagnetic anomalies [*Grauch and Hudson*, 2007], this model shows that the magnetic anomaly (RTP-TMI) above the fault is steepest in the direction of fault dip, and that buried faults are typically characterized by double-peak horizontal gradient magnitude.

We delineate the edges of buried basement faults by the 0° tilt-angle derivative contour [*Salem et al.*, 2007]. In map view, the 0° tilt-angle contour typically delineates the footwall cut-off of a normal fault and wraps around the top of the footwall block [e.g., *Fairhead et al*., 2010]. The determination of the segment of the contour that correspond to the actual footwall cut-off edge is based upon other sources of dip-direction information (e.g. field data, seismological data, geometry of the RTP-TMI on opposite sides of the anomaly) related to the target structure. Also, we observe that the 0° tilt-angle contour roughly corresponds to the boundary between high and low gradients along the trend of the magnetic lineaments on other derivative maps (e.g., Dz and Dy). Therefore, on our derivative maps (excluding the tilt-angle derivative), we interpret the approximate trace of faults along the edge of target magnetic lineaments.

We estimated depths to the top of the magnetic sources (i.e. basement) using the Source Parameter Imaging (SPI) method [*Smith et al.*, 1998; *Smith and Salem*, 2005]. Depth calculations from aeromagnetic data have an accuracy of ±20% [*Gay,* 2009]. Our basement depth estimates at the edge of buried structures were also consistent with estimates from the tilt-depth method of *Salem et al.* [2007]. We estimated the dip angle of the earthquake ruptured fault from the angular relationship between the locations of the 0° tilt-angle at the basement level (at depth) and the coseismic fault ruptures at the ground surface and compare our result with previously published estimates from *Biggs et al.* [2010] and *Hamiel et al.* [2012]. We produce a 2-D aeromagnetic geological section from the depth-to-basement analysis of the 2013 high resolution magnetic data using the SPI technique, tilt-angle derivative, and surface topography estimates from the Near-Global 1-arcsecond SRTM-DEM data (30 m spatial resolution). For areas with thick sedimentary cover, we subset the aeromagnetic map within such areas (ensuring that large magnetic anomalies are not included in the subset) and applied the tilt-angle and directional derivative filters in order to enhance the signals of subtle basement fabric obscured by the thick sedimentary cover and presence of large magnetic anomalies in the vicinity.

5. Results

5.1. Filtered aeromagnetic maps

The first order vertical derivatives of the 1984-1985 and 2013 RTP aeromagnetic data reveal details of the crystalline basement fabric related to the MSZ which are represented by high frequency, short wavelength WNW-NW-trending lineaments of high and low magnetic gradients, especially apparent northwest and southwest of Karonga town (‘MSZ’ in Figures 4, S1a and b).

The lineaments are also visible in the north, west and southwest of Kaporo town (Figure 4). However, around Karonga town, the high frequency aeromagnetic lineaments are obscured by lower frequency, longer wavelength NNW-trending magnetic anomalies (Figure 4). Northwest of Karonga town, within the Ruwenya-Misuku Mountains, the high frequency MSZ magnetic fabric defines a WNW-trending (125°) ~22 km-wide zone, that is truncated by a N-S trending curvilinear magnetic discontinuity compares very well with the location and geometry of the Karonga Fault in previously published geologic map of the area (KF in Figure 3a). We observe that numerous normal faults exposed in the basement outcrops around the Karonga area (Figure 3a) coincide with these NNW-trending lower frequency, longer wavelength magnetic lineaments. For example, the west-dipping normal faults bounding Yembe Hill (just west of Kaporo) and Mbiri Hill (at Chilumba) to the west (Figure 4). Therefore, we interpret the lower frequency, longer wavelength magnetic gradients to represent buried and subaerial basement-rooted normal faults bounding asymmetrical grabens and half-grabens filled with sedimentary rocks.

In Figure S2a-d, we show various characteristics of these buried faults in Karonga area as enhanced by different derivative filters. The RTP Total Magnetic Intensity (RTP-TMI) map (Figure S2a) shows the long wavelength, low frequency character of the buried faults (KPF, SMF, KTF and LF), as well as the short wavelength, high frequency of the MSZ-related magnetic lineaments. The horizontal-Y derivative (Dy) of the RTP-TMI map (Figure S2b) reveals the ~E-W discontinuities along the strike of each of the ~N-S striking lineaments (i.e. segmentation and changes in the strike of the lineaments). The vertical derivative (Dz) map also clearly reveals the geometry of the magnetic lineaments representing the faults (Figure S2c). Although the tilt-angle derivative shows the geometry of the edge of the faults (0° tilt-angle contour; Figure S2d), for subaerial faults that intersect high amplitude magnetic fabric in exposed basement rocks (e.g. the

Karonga Fault, KF), the tilt-angle contour of the fault trace is intermittently deflected by that of the interfering basement magnetic fabric along-strike of the fault. From the filtered aeromagnetic maps, we find five major normal faults buried beneath rift sediments along the half-graben hinge zone and these are named St. Mary Fault (SMF), Kaporo Fault (KPF), Katesula Fault (KTF), Lupaso Fault (LF) and Mbiri Fault (MF) (Figures 4, S1, S2 and S3). The LF and KTF extend in a northwest direction for ~19 km, SMF for 37 km and KPF for 36 km. The SMF, LF, KTF and MF are within the coastal plain sediments whereas the KPF is offshore beneath Lake Malawi (Figure 4). The 62 km-long Mbiri Fault (MF), for the most part is buried beneath the coastal plain sediments but crops out in the Chilumba town where it bounds the Mbiri Hill in the west. Only the northernmost segment of the SMF outcrops west of Kaporo town where it bounds the Yembe Hill in the west (Figure 4).

Within the basin fill on the hanging walls of the SMF and KPF, we observe low amplitude, high frequency, short wavelength magnetic lineaments enhanced on the tilt-angle derivative map due to the normalizing effect of the tilt-angle derivative operator (Figure 5a; white arrows in Figure 5b). In order to further enhance the edges associated with these 'suppressed' lineaments (low amplitude) and better observe their geometrical trends, we first subset out the tilt-angle derivative grid covering the target area, ensuring that we avoid the higher amplitude anomalies associated with exposed basement rocks (areas west of Karonga Fault) and buried basement-rooted normal faults (e.g., KPF, KTF and the southern segment of the SMF). Following this, we applied a directional derivative (45º directional gradient) to the subset map to enhance the edges associated with the 'suppressed' lineaments. We then overlaid the filtered subset on the tilt-angle derivative using transparency (Figure 5c). The resultant map (Figure 5c) reveal the overall geometry of the suppressed lineaments. The filtered map shows that the 'suppressed' lineaments (e.g., see black

arrows in Figure 5c) align with the NW-trending MSZ magnetic fabric in the exposed basement northwest of Karonga town (in the Ruwenya-Misuku Mountains). Overall, we observe that the MSZ magnetic lineaments strike WNW (125°) northwest of Karonga town, but gradually rotates into a NNW (149°) strike northeast and east of the town (Figure 5b). In addition, the overall trend of the enhanced 'suppressed lineaments' to north and east of Karonga town is consistent with the trend of the magnetic lineaments of the MSZ outcrops southwest of the Karonga town ("MSZ" in Figure S3a and b). The above observations suggest that the 'suppressed' magnetic lineaments represent the continuation of the trend of the MSZ-related magnetic lineaments in the basement beneath the asymmetrical grabens and half-grabens. South of the Karonga area and all the way to the Chilumba town, the MSZ-related magnetic lineaments change to NW (135°) trend (shown by white arrows in Figure S1a and b).

Although, the segmentation (side-stepping and strike-deflection characteristics) of fault-related lineaments are readily observable on the vertical derivative maps, we used the directional derivatives of the vertical derivative to enhance the subtle along-strike and across-strike discontinuities. Figure 6 illustrates the across-strike discontinuities (side-stepping characteristics) along some of the identified basement-rooted normal faults, revealed by the application of horizontal-X derivative (Dx) filter to the vertical derivative of the 2013 aeromagnetic data. We also observe distinct changes in the fault strike along the northern segment of the SMF in the horizontal-Y derivative of the RTP-TMI (Dy) (black arrows in Figure S2b) and tilt-angle derivative (black arrows in Figure S2d).

5.2. Distribution of earthquake surface ruptures

A plot of the locations of the 2009 Karonga earthquake surface ruptures indicates an NNW-trending zone which extend over a total length of 16.4 km (Figure S3a and b). The mapped surface rupture locations follow the SMF magnetic lineament; however, the surface ruptures only cover about half the length of the lineament. The SMF magnetic lineament is clearly observable on both the 1984-1985 and 2013 aeromagnetic data.

5.3. Geological cross-section

The edges of basement structures (0° tilt-angle contour) are revealed by the tilt-angle derivative of the aeromagnetic grid (Figures S2d), while the SPI maps (Figure 7a and b) show the estimate of depth to magnetic source (crystalline basement) within the sedimentary basin. We combine these basement models with surface topography to generate two aeromagnetic geological sections across mapped buried faults along the half-graben hinge zone (cross-sections A'-B'-C'-D' in Figures 8a-d, and E'-F' in Figures 9a-d). Here, the magnetic-high RTP-TMI anomalies over the faults are steeper to the west than to the east (Figures 8b and 9b). Along the SMF, the basement footwall cutoff is located at 508 m (in the south; Figure 8d) and 413 m (in the north; Figure 9d) depths beneath the Cenozoic lacustrine sediments. Whereas, along the KPF, the footwall cut off is at 1,017 m (in the south; Figure 8d) and 748 m (in the north; Figure 9d) depths. Along the SMF and KPF, depth-to-basement generally decreases northwards. The depth-to-basement models show distinct topographic highs immediately east of the faults. Based on the angular relationship between the locations of the 0° tilt-angle (at the basement level) and coseismic fault ruptures at the ground surface, we interpret a 50° dip angle for the SMF (along section A'-B'-C'-D') (Figure 8d). On the sensitivity of our dip angle estimate for the SMF, an accuracy of ±20% [*Gay,* 2009] for its 508 m

footwall cut-off depth (using the SPI technique, Figure 8c) gives a range of 44°–55° dip angles. This estimate is consistent with previously published dip estimates from fault plane solutions and DInSAR analyses of coseismic events [37°−46° from *Biggs et al.*, 2010, and 41° from *Hamiel et al.*, 2012]. In the absence of information on possible coseismic ruptures along the Kaporo Fault (buried beneath the lake), we infer the same dip angle as the St. Mary Fault. Also, the cross-sections show a general eastward (basinward) decrease in basement elevation (Figures 8d and 9d) similar to previously published basement models of the North Basin [*Mortimer et al.*, 2007; *Biggs et al*., 2010], we suggest that the depth-to-basement estimates are reliable within an accuracy of ±20%.

6. Discussion

6.1. Relationship between surface rupture locations and magnetic lineaments

The mapped surface rupture locations from the 2009 Karonga earthquake align along the edge of the distinct ~37 km long, 148°-162° striking SMF magnetic lineament in the basement that is apparent on both the pre-earthquake (1984-1985 data) and post-earthquake (2013 data) aeromagnetic maps (black arrows on Figure S1a-b; S3a-b). This demonstrate that the SMF (St. Mary Fault) is imaged prior to the 2009 earthquake sequences, indicating that the SMF predates the earthquake. Therefore, we suggest that the 2009 Karonga earthquake was associated with the reactivation of a pre-existing buried basement-rooted fault that we mapped as the SMF (Figure 4, 7a and b). The RTP-TMI anomaly over the SMF and KPF is typical of buried basement-rooted normal faults in areas where the crystalline basement is the dominant magnetic source [*Grauch and Hudson*, 2007; 2011], such that the magnetic anomaly is steepest in the direction of fault dip.

The RTP-TMI anomalies over the faults are steeper to the west than to the east (Figures 8b and 9b), suggesting a west-dip for the faults and is consistent with DInSAR analyses of the earthquake [*Biggs et al.*, 2010; *Hamiel et al.*, 2012]. This dip direction indicates the faults are synthetic to the Livingstone border Fault.

Figures S2b shows along-strike changes in the geometry of the fault-related magnetic lineaments (i.e. change in strike direction), and Figure 6 shows 'across-strike' variation in the trend of the lineaments (i.e. side-stepping characteristics). On Figure 6, we illustrate the trace of the fault segments along the edges of each distinct segment. We observe that the segmentation of the magnetic lineament corresponding to the SMF is such that the middle segment of the lineament has a distinct right-stepping ~1 km-wide relay ramp across which the coseismic surface ruptures also show along-strike right-stepping pattern (Zone-2 in Figure 6). Previous studies [e.g. *Cartwright et al*., 1995; *Fossen*, 2010] have shown that fault growth and propagation involve an initial nucleation of isolated fault segments, followed by overlapping of segments separated by relay ramps, and eventual bridging of relay ramps to allow the geometrical linkage and coalescence of the fault segments. Zone-1 of Figure 6 shows that the southern segment of the SMF (south of Karonga town) consists of coalesced right-stepping fault segments. However, north of Karonga, the fault is characterized by overlapping segments separated by a relay ramp along which the earthquake surface ruptures align (Zone-2 in Figure 6). Farther north, the SMF is characterized by weakly resolved, subtle NW aeromagnetic trends (dotted lines in Zone-3 of Figure 6), not corresponding to specific faults, in contrast to the southern segments where fault-related features are well resolved (solid lines in Zones-1 and 2). Therefore, in the poorly-resolved northern segments, we rely on fault interpretation from Dy of the vertical derivative (Figure S2b). Black arrows in Figure S2b along the northern segment of SMF suggest that this part of the fault is

characterized by en échelon right-stepping segments with wider relay ramps. The propagation of the earthquake surface ruptures along overlapping fault segments and across the intervening relay ramp north of Karonga (Zone-2 of Figure 6) indicates that the rupture of the 2009 Karonga earthquake is associated with active deformation of the relay ramp that might ultimately lead to coalescence of fault segments along the SMF. Also, we interpret that the amplitude of the magnetic anomaly representing the SMF is significantly lower in the north (zone-3) than in the south (zone-1) (Figures S2a-b, S3 and 6) possibly due to the dominance of unlinked fault segments and shallower basement depths (and lower fault dips or lower vertical fault throws?) in the north relative to the middle and southern segments of the fault (Figures 8d and 9d). This may also explain the poor resolution of fault segmentation in Zone-3 of Figure 6. In addition, coalesced nature of fault segments in the southern part of the SMF, and the presence of relay ramps between segments in the central part of the fault and even wider relay ramps between segments in the northern portion of the fault may indicate that the 2009 earthquake event was associated with an overall northward growth of the southern segment of the fault.

We have also identified other NW, N-S and NNW-striking faults beneath the onshore area of Lake Malawi; such as KPL, KTF and LF extending from Kaporo in the north to Chilumba to the south (Figure 7b). Unpublished hypocentral relocation of the 2009 Karonga earthquake events confirm ruptures along the SMF and the KPF (personal communication, James B. Gaherty, 2017). We highlight these faults as additional buried basement-rooted faults which bound asymmetrical grabens and half-grabens. We also observe that these buried faults are synthetic to the Livingstone Fault (i.e. west-dipping), except the Lupaso Fault that dips eastward and appear to be a southward continuation of the Karonga Fault. The westward dips of most of these faults is consistent with the dip direction of majority of the hanging wall faults interpreted in previous seismic studies within

the North Basin [*Specht and Rosendahl*, 1989; *Scholz and Finney*, 1994; *Mortimer et al*., 2007]. We observe that the basement top is located at deeper depths at the hanging wall of the KPF compared to that of the SMF, thus suggesting that the KPF may have accommodated more displacement than other buried faults in the Karonga area (Figure 8d and 9d). This fault has a segmentation pattern similar to the SMF where NW-striking segments seem to overlap to form a NNW-SSE striking fault (Figure 6).

6.2. Relationship between basement structures and the Mughese Shear Zone (MSZ) fabric

The strike of the SMF changes from NNW in the south to N-S to the north (black arrow in Figure S1b points to the location of strike deflection). On the other hand, the strike of the MSZ-related magnetic lineaments changes from NW in the north to NNW in the southeast (Figure 5a-b). This gives an apparent impression that only the southern half of the SMF aligns with the NNW-striking segment of the MSZ, while its northern half cuts across the trend of the MSZ. However, detailed delineation of the orientation of segments of the SMF reveals that its northern half is made-up of several short en échelon NW-NNW-striking fault segments (black arrows in Figures S2b). We observe that the strike of one of these short en échelon segments is consistent with the nodal planes on the fault plane solution of one of the seismic events (southernmost fault plane solution in Figures S2b and 5c) associated with the 2014 M_w 5.1 Karonga earthquake sequence [*Oliva et al.*, 2016]. The nodal plane also lines up with the strike of MSZ fabric just northwest of the epicenter. The strike-slip fault plane solution in the north is possibly associated with slip on a transfer fault that links two normal faults [*Oliva et al.*, 2016]. The southern half of the SMF, however, is made up of longer en échelon NNW-striking segments that appear to align along NNW-trending fabric

of the MSZ (Figures 5b-c and S3b). The southern segments of the SMF show coalescence while its northern segments might eventually coalesce to form a more penetrative N-trending fault. The coalescence of fault segments that originally reactivated the MSZ basement fabric results in an overall fault geometry that appears to cut obliquely across the MSZ basement fabric. Based on the enhanced trend of the MSZ-related lineaments underlying the sedimentary cover (Figures 5b-c), and interpreted the map-view geometry of the buried KPF and SMF faults (Figures S2b, S2d and 6), we interpret an alignment of segments of the faults with the southeast continuation of the MSZ basement fabric (Figure 10). The trend of the MSZ switches from NW-strike in the northwest to a NNW-strike in the Karonga area and back to a NW-strike in the southeast between Karonga and Chilumba towns (white lines in Figure 10). This indicates a subtle right-stepping bend of the MSZ. The trend of the magnetic anomalies manifesting the southwestern boundary of the shear zone also suggests this geometry (white arrows in Figure S1a and b). It is not surprising that north of Karonga town, the MSZ fabric is subtly imaged in the high resolution aeromagnetic data as the fault offsets are probably not large (Figure 9) and within magnetic basement in contrast to the more rift parallel southern segments of the SMF and KPF which have accommodated larger offset in the magnetic basement and magnetite poor sedimentary rocks (Figure 8). Therefore, the alignment of segments of the SMF, KPF, KTF, LF and MF with the MSZ fabric suggest that these faults exploited the basement fabric. Farther south of Karonga town, the reactivation of the southeastern segment of the MSZ is shown by the alignment of magnetic lineaments with the MF which crops out at Chilumba town and bounds the Mbiri Hill in the west (Figure 4 and 10). Although the presence of Permo-Triassic sedimentary rocks along the scarp of the KF suggests that the fault is related to Karoo rifting (Figure 3a), we suggest that a better understanding of the syntectonic stress-field may provide insight into the mechanics of propagation of the fault across the fabric of the MSZ.

Studies [e.g. *Bell*, 1996; *Zang and Stephansson*, 2010; *Morley*, 2010] have shown that geomechanical property contrasts can cause local reorientation of stresses (herein referred to as stress rotations), such that where the discontinuity is relatively weak the maximum principal stress and maximum horizontal stress (S_{Hmax}) directions will deflect sub-parallel to the discontinuity. Where the material is relatively strong (stiff), the maximum principal stress and S_{Hmax} will deflect sub-perpendicular to the discontinuity. *Morley* [2010] demonstrated that basement domains with well-defined metamorphic foliation and mylonitic fabric are zones where stress rotations can occur. In northern Malawi, although it is suggested that the direction of regional extension has changed over time [e.g. *Ring*, 1994; *Mortimer* et al., 2007], the E-W present-day extension direction [*Saria et al.*, 2014] is sub-orthogonal to the overall trend of the SMF (White arrows in Figure 10). Therefore, we suggest that the obliquity of the SMF with respect to MSZ basement fabric is effectively controlled by local stress rotations from the regional E-W extension direction into a plane that is sub-orthogonal to the trend of the MSZ fabric. Thus, the stress rotation is locally resolved as normal displacement reactivating obliquely-oriented basement fabric.

Previously published DInSAR models of the 2009 Karonga earthquake [*Biggs et al.*, 2010; *Hamiel et al*., 2012] and our modeling of depth-to-magnetic-source (crystalline basement) from high resolution aeromagnetic data (Figure 8d) reveal a 37°-50° SW dip angle for the ruptured faults (SMF and other faults along the half-graben hinge zone). Although we observe that the faults follow basement fabric along-strike, the estimated dip angle of the faults are shallower than the relatively steeper sub-vertical dip angles (60°-85°) of the MSZ basement fabric [Figures 3b and c; *Ring*, 1993]. Several studies have reported the development of younger faults parallel to the strike of basement fabric, which cut this fabric obliquely down-dip [e.g. *Morley*, 1995; *Ring et al*., 2005; *Morley*, 2010]. *Morley* [2010] observed low-angle (20°-30°) normal faults reactivating along

basement foliation within the Rukwa Rift, and attributed the fault development to stress rotations; such that the dip angle defining the least cohesive shear strength for the propagation of the normal faults was 30° away from the rotated maximum principal stress (dip of the foliation). We suggest that the reactivation of the MSZ basement fabric into normal faults that follow the fabric along strike but develop into a lower-angle fault down-dip can be explained by the stress-rotation model of *Morley* [2010]. According to this model, the normal fault that subsequently develops from reactivation by stress rotations will appear to obliquely cut foliation down dip with at angular difference of ~30°. Based on this model, the 60°-85° dips of the MSZ basement fabric in the Karonga area should reactivate into normal faults with ~30°-55° dip angles, thus explaining the relatively shallow 37°-50° dip angle of the buried basement faults in Karonga area as compared to the steeper dip angles of the MSZ basement fabric.

6.3. Half-graben hinge zone deformation

Figures 11a and b shows the spatial distribution of the earthquake epicenters associated with the 2009 Karonga seismic event. This distribution shows that the majority of the earthquakes cluster in the region bounded by the KPF in the east, the KF to the west, and the area just west of the LF where the MSZ outcrops (area bounded by the dashed white ellipse in Figure 11a). We suggest that although most of the $M_w \geq 4.9$ events as well as significant ground displacement during the 2009 earthquake swarm were localized along the SMF, the other identified buried basement faults underlying the Karonga area (KPF, KTF, LF and MF) might have also accommodated some of the deformation. In addition, the spatial distribution of epicenters with respect to the entire North Basin of the Malawi Rift suggests that active deformation associated with the 2009 seismic events is

localized within the half-graben hinge zone (Figure 11b) and not distributed across the entire hanging-wall as suggested by *Biggs et al*. [2010]. The location of seismic events west of the east-dipping KF (Figure 11a and b) may suggest that the planes of the SMF and KPF (west-dipping) undercut the KF down-dip, thereby highlighting the need to better understand the subsurface interaction of the faults along the half-graben hinge zone.

Models proposed for the development of half-graben rift basins generally assume that the hinge zones of half-grabens are mainly flexural margins with brittle deformations that develop passively in response to progressive displacement along the border fault [e.g. *Rosendahl et al*., 1986; *Groshong*, 1989; *Schlische*, 1991; *Seyitoglu et al*., 2002]. We alternatively suggest that the localization of upper crustal strain and seismicity on the half-graben hinge zone of the North Basin in the weakly extended, magma-poor Malawi Rift is not entirely driven by a passive crustal flexure of the border fault hanging-wall, but is being facilitated by the presence of favorably-oriented basement fabric. We further suggest that the influence of the MSZ on the large-scale structural architecture of the North Basin may be most evident in the relatively lower dip angles of the hinge zone faults (<50°) compared to that of the intrabasin faults and border fault (55° - 60°; *Wheeler and Karson*, 1989; *Mortimer et al.*, 2007) (Figure 11b).

6.4. Implications for earthquake hazards

Our study shows that the surface ruptures occurred mostly along the central part of the SMF with a total length of 16.4 km, covering half the length of the 37 km-long fault (Figures S3 and 6). We point to the high potential for frequent brittle failure along the unruptured, soft-linked, en échelon northern segments of the SMF between Karonga and Kaporo towns in the future (Zone-3 in Figure

6). The presence of longer fault segments on the southern part of the SMF (Zone-1 in Fig. 6) relative to its northern segments (Zone-3 in Fig. 6) suggest that the southern segment of the SMF is capable of bigger earthquakes if it were to rupture. The fact that the southern segment has not ruptured recently may indicate that it is a seismic gap with potential of future rupture. Following standard scaling magnitude-length relationship [e.g., *Wells and Coppersmith*, 1994; *Field et al*., 2003], an earthquake of $M_w 6.4 \pm 0.34$ (mean magnitude) could occur if this entire 'seismic gap' were to rupture in a single event. Overall, due to the presence of en échelon segmentation of the SMF in the north than in the south, we predict a relatively higher probability for frequent seismic activities in the northern part of Karonga area than in the south. This prediction is supported by the M_w 5.1 2014 Karonga earthquake sequence reported by *Oliva et al.* [2016]. The epicenters of this earthquake event were located ~3 km west and 5 km SW of Mwenitete town (yellow stars in Figure 11a); however, hypocentral depths of 5-10 km suggest that the rupture possibly occurred down-dip of the SMF and/or KPF. We also raise the possibility that the extents of the KPF, KTF, LF and MF present favorable sites for future brittle rupture leading to seismic activities along the half-graben hinge zone. We present an updated fault map of the North Basin, showing the possible seismogenic faults along the half-graben hinge zone (Figure 12). We observe that the faults interpreted from aeromagnetic data in this study (red lines in Figure 12) compares very well with the fault lines reported from previously-published seismic interpretations of the North Basin (yellow lines in Figure 12) [*Specht and Rosendahl*, 1989; *Scholz and Finney*, 1994; *Mortimer et al*., 2007].

7. Conclusions

We documented for the first time, the presence of seismogenic buried basement faults along the half-graben hinge zone that could potentially be sites of future brittle rupture that will trigger earthquakes. From the analysis of pre-earthquake and post-earthquake aeromagnetic data and field observation, we delineated the along-strike geometry and dip angle of the SMF that ruptured during the 2009 Karonga earthquake. We also identified other potential seismogenic buried faults in the area and showed that the recent seismicity along the ruptured SMF is associated with overall northward development of the SMF, and geometrical linkage and coalescing of initially overlapped segments. In addition, we suggest the reactivation of sub-vertical basement fabric along the North Basin half-graben hinge zone by stress rotation. Fault geometries, basement fabric analyses, and spatial distribution of recent seismicity in the magma-poor, weakly-extended northern Malawi Rift suggest that focusing of upper crustal deformation leading to moderate-magnitude seismicity along the half-graben hinge zone may not be entirely driven by crustal flexure, but may also be facilitated and modulated by the MSZ basement fabric. Careful analysis of aeromagnetic data can play an important role in delineating causative faults associated with damaging seismic events and can therefore help earthquake mitigation efforts.

Acknowledgements

This work was partially supported by the National Science Foundation (NSF) grant EAR10-09988 to E.A. Atekwana. We thank the Geological Survey Department of Malawi for allowing us to purchase the 2013 aeromagnetic data used in this study. We have archived the 2013 aeromagnetic data for the Karonga area at the GeoPRISMS data portal (DOI: 10.1594/IEDA/324314). We thank the Council for Geosciences, South Africa for providing the old (1984/85) aeromagnetic data used

in this study. We have also archived the 1985 aeromagnetic data for the Karonga area at the GeoPRISMS data portal (DOI: 10.1594/IEDA/324312). The Council for Geosciences, South Africa can be reached through info@geoscience.org.za. We also thank two anonymous reviewers for detailed and constructive reviews. This is the Oklahoma State University Boone Pickens School of Geology contribution no. 2018-80.

References

Arkani-Hamed, J. (1988), Differential reduction-to-the-pole of regional magnetic anomalies, *Geophysics*, *53*, 1592–1600.

Baranov, V. (1957), A new method for interpretation of aeromagnetic maps: Pseudo-gravimetric anomalies, *Geophysics*, *22*, 359-383.

Beacom, L. E., R. E. Holdsworth, K. J. W. McCaffrey, and T. B. Anderson (2001), A quantitative study of the influence of pre-existing compositional and fabric heterogeneities upon fracture-zone development during basement reactivation, *Geol. Soc., London, Spec. Pub.*, *186*(1), 195-211.

Bell, J. S. (1996), In situ stresses in sedimentary rocks (part 2): applications of stress measurements. *Geosci. Can.*, *23*(3), 135–153.

Biggs, J., E. Nissen, T. Craig, J. Jackson, and D. P. Robinson (2010), Breaking up the hanging wall of a rift-border fault: the 2009 Karonga earthquakes, Malawi, *Geoph. Res. Lett.*, *37*, L11305.

Bott, M. H. (1997), Modeling the formation of a half graben using realistic upper crustal rheology, *J. Geoph. Res.: Solid Earth*, 102(B11), 24605-24617.

Calais, E., N. d'Oreye, J. Albaric, A. Deschamps, D. Delvaux, J. Déverchere, C. Ebinger, R. W. Ferdinand, F. Kervyn, A. S. Macheyeki, and A. Oyen (2008), Strain accommodation by slow slip and dyking in a youthful continental rift, East Africa, *Nature, 456*(7223), 783-787.

Carter, G. S., and J. D. Bennett (1973), The geology and mineral resources of Malawi (2nd revised edition), *Geol. Surv. of Malawi Bull.*, *6*, 62.

Cartwright, J. A., B. D. Trudgill, and C. S. Mansfield (1995), Fault growth by segment linkage: an explanation for scatter in maximum displacement and trace length data from the Canyonlands Grabens of SE Utah, *J. Struct. Geol., 17*(9), 1319-1326.

Castaing, C. (1991), Post-Pan-African tectonic evolution of South Malawi in relation to the Karroo and recent East African rift systems, *Tectonophysics*, *191*(1-2), 55-73.

Chorowicz, J. (2005), The East African rift system, *J. African Earth Sci., 43*, 379–410.

Cooper, G. R. J., and D. R. Cowan (2006), Enhancing potential field data using filters based on the local phase, *Computers & Geosciences*, *32*(10), 1585-1591.

Corti, G., J. van Wijk, S. Cloetingh, and C. K. Morley (2007), Tectonic inheritance and continental rift architecture: Numerical and analogue models of the East African Rift system, *Tectonics*, *26*(6).

Craig, T. J., J. A. Jackson, K. Priestley, and D. McKenzie (2011), Earthquake distribution patterns in Africa: their relationship to variations in lithospheric and geological structure, and the rheological implications, *Geoph. J. Int.*, *185*, 403-434.

Daly, M. C. (1988), Crustal Shear Zones in Central Africa：a Kinematic Approach to Proterozoic Tectonics, *Episodes*, *11*(1), 5-11.

Daly, M. C., J. Chorowicz, and J. D. Fairhead (1989), Rift basin evolution in Africa: the influence of reactivated steep basement shear zones, *Geol. Soc., London, Special Publications*, *44*(1), 309-334.

Dawson, S. M., D. A. Laó-Dávila, E. A. Atekwana, and M. G. Abdelsalam (2018), The influence of the Precambrian Mughese Shear Zone structures on strain accommodation in the northern Malawi Rift, *Tectonophysics*, 722, 53-68.

Ebinger, C. J., and M. Casey (2001), Continental breakup in magmatic provinces: An Ethiopian example, *Geology*, *29*(6), 527–530.

Ebinger, C. J., A. L. Deino, R. Drake, and A. L. Tesha (1989), Chronology of volcanism and rift basin propagation: Rungwe Volcanic Province, East Africa, *J. Geophys. Res.*, *94*, 15785–15803.

Fairhead, J. D., A. Salem, and R. J. Blakely (2010), Continental to basin scale mapping of basement depth and structure using the tilt-depth method, In *EGM 2010 International Workshop*.

Fagereng, Å. (2013), Fault segmentation, deep rift earthquakes and crustal rheology: Insights from the 2009 Karonga sequence and seismicity in the Rukwa–Malawi rift zone, *Tectonophysics*, *601*, 216-225.

Field, E. H., T. H. Jordan, and C. A. Cornell (2003), OpenSHA: A developing community-modeling environment for seismic hazard analysis, *Seis. Res. Lett*., *74*(4), 406-419.

Fossen, H. (2010), Structural Geology, *Cambridge Univ. Press, New York*, 463.

Gay Jr., S. P. (2009), Reactivation tectonics: The evidence and the consequences, American Stereo Map Co., Salt Lake City, Utah.

Goldsworthy, M., and J. Jackson (2001), Migration of activity within normal fault systems: Examples from the Quaternary of mainland Greece, *J. Struct. Geol.*, *23*, 489–506.

Grauch, V. J. S., and M. R. Hudson (2007), Guides to understanding the aeromagnetic expression of faults in sedimentary basins: Lessons learned from the central Rio Grande rift, New Mexico, *Geosphere*, *3*(6), 596-623.

Grauch, V. J. S., and M. R. Hudson (2011), Aeromagnetic anomalies over faulted strata, *The Leading Edge*, *30*(11), 1242-1252.

Groshong, R. H. (1989), Half-graben structures: Balanced models of extensional fault-bend folds, *Geol. Soc. of Amer. Bull.*, *101*(1), 96-105.

Hamiel, Y., G. Baer, L. Kalindekafe, K. Dombola, and P. Chindandali (2012), Seismic and aseismic slip evolution and deformation associated with the 2009–2010 northern Malawi earthquake swarm, East African Rift, *Geophys. J. Int.*, *191*, 898–908.

Hussein, H. M., I. Marzouk, A. R. Moustafa, and N. Hurukawa (2006), Preliminary seismicity and focal mechanisms in the southern Gulf of Suez: August 1994 through December 1997, *J. Afr. Earth Sci.*, *45*(1), 48-60.

Jacobs, L. L., D. A. Winkler, Z. M. Kaufulu, and W. R. Downs (1990), The dinosaur beds of northern Malawi, Africa, *Nat. Geo. Res.*, *6*(2), 196-204.

Katumwehe, A. B., M. G. Abdelsalam, and E. A. Atekwana (2015), The role of pre-existing Precambrian structures in rift evolution: The Albertine and Rhino grabens, Uganda, *Tectonophysics*, 646, 117-129.

Kearey, P., K. A. Klepeis, and F. J. Vine (2009), Global Tectonics, *John Wiley & Sons*.

Kinabo, B. D., E. A. Atekwana, J. P. Hogan, M. P. Modisi, D. D. Wheaton, and A. B. Kampunzu (2007), Early structural development of the Okavango rift zone, NW Botswana, *J. of Afric. Earth Sci.*, *48*, 125-136.

Kinabo, B. D., J. P. Hogan, E. A. Atekwana, M. G. Abdelsalam, and M. P. Modisi (2008), Fault growth and propagation during incipient continental rifting: insights from a combined aeromagnetic and Shuttle Topography Mission digital elevation model investigation of the Okavango Rift Zone, northwest Botswana, *Tectonics*, *27*, 1-16.

Laó-Dávila, D. A., H. S. Al-Salmi, M. G. Abdelsalam, and E. A. Atekwana (2015), Hierarchical segmentation of the Malawi Rift: The influence of inherited lithospheric heterogeneity and kinematics in the evolution of continental rifts, *Tectonics*, *34*, 2399–2417.

Leseane, K., E. A. Atekwana, K. L. Mickus, M. G. Abdelsalam, E. M. Shemang, and E. A. Atekwana (2015), Thermal perturbations beneath the incipient Okavango Rift Zone, northwest Botswana, *J. Geoph. Res*., *120*, 1210-1228.

Ma, G. Q., X. J. Du, L. L. Li, and L. S. Meng (2012), Interpretation of magnetic anomalies by horizontal and vertical derivatives of the analytic signal, *Appl. Geoph.*, *9*(4), 468-474.

Macheyeki, A. S., H. Mdala, L. S. Chapola, V. J. Manhiça, J. Chisambi, P. Feitio, A. Ayele, J. Barongo, R. W. Ferdinand, G. Ogubazghi, and B. Goitom (2015), Active fault mapping in Karonga-Malawi after the December 19, 2009 Ms 6.2 seismic event, *J. of Afr. Earth Sci.*, *102*, 233-246.

McCartney, T., and C. A. Scholz (2016), A 1.3 million year record of synchronous faulting in the hanging wall and border fault of a half-graben in the Malawi (Nyasa) Rift, *J. Struct. Geol*., *91*, 114-129.

Miller, H. G., and V. Singh (1994), Semiquantitative techniques for the removal of directional trends from potential field data, *J. Appl. Geoph*., *32*, 199-211.

Modisi, M. P., E. A. Atekwana, A. B. Kampunzu, and T. H. Ngwisanyi (2000), Rift kinematics during the incipient stages of continental extension: evidence from the nascent Okavango rift basin, northwest Botswana, *Geology*, 102, 363-376.

Morley, C. K. (1995), Developments in the structural geology of rifts over the last decade and their impact on hydrocarbon exploration, *Geol. Soc., London, Special Publications*, *80*(1), 1-32.

Morley, C. K. (2010), Stress re-orientation along zones of weak fabrics in rifts: An explanation for pure extension in ‘oblique’ rift segments?, *Earth and Planet. Sci. Lett.*, *297*(3), 667-673.

Morley, C. K., C. Haranya, W. Phoosongsee, S. Pongwapee, A. Kornsawan, and N. Wonganan (2004), Activation of rift oblique and rift parallel pre-existing fabrics during extension and their effect on deformation style: examples from the rifts of Thailand, *J. Struct. Geol.*, *26*(10), 1803-1829.

Mortimer, E., D. A. Paton, C. A. Scholz, M. R. Strecker, and P. Blisniuk (2007), Orthogonal to oblique rifting: effect of rift basin orientation in the evolution of the North basin, Malawi Rift, East Africa, *Basin Res.*, *19*(3), 393-407.

Mortimer, E.J., D. A. Paton, C. A. Scholz and M. R. Strecker (2016a), Implications of structural inheritance in oblique rift zones for basin compartmentalization: Nkhata Basin, Malawi Rift (EARS), *Mar. Petrol. Geol*., *72*, 110-121.

Mortimer, E., L. A. Kirstein, F. M. Stuart, and M. R. Strecker (2016b), Spatio-temporal trends in normal-fault segmentation recorded by low-temperature thermochronology: Livingstone fault scarp, Malawi Rift, East African Rift System, *Ear. Plan. Sci. Lett.*, *455*, 62-72.

Moussa, H. H. M. (2008), Spectral P-wave magnitudes, magnitude spectra and other source parameters for the 1990 southern Sudan and the 2005 Lake Tanganyika earthquakes, *J. Afr. Earth Sci*., *52*(3), 89-96.

Muirhead, J. D., S. A. Kattenhorn, H. Lee, S. Mana, B. D. Turrin, T. P. Fischer, G. Kianji, E. Dindi, and D. S. Stamps (2016), Evolution of upper crustal faulting assisted by magmatic volatile release during early-stage continental rift development in the East African Rift, *Geosphere, 12*(6), 1670-1700.

Oliva S. J. C., C. J. Ebinger, D. Keir, D. J Shillington, and P. R. N. Chindandali (2016), Deciphering the role of fluids in early stage rifting from full moment tensor inversion of East African earthquakes, *American Geophysical Union (AGU) 2016 meeting* poster T51C-2942.

Phillips, T. B., C. A. Jackson, R. E. Bell, O. B. Duffy, and H. Fossen (2016), Reactivation of intrabasement structures during rifting: A case study from offshore southern Norway, *J. of Struc. Geol.*, *91*, 54-73.

Ring, U. (1993), Aspects of the kinematic history and mechanisms of superposition of the Proterozoic mobile belts of eastern Central Africa (northern Malawi and southern Tanzania), *Precambrian Res.*, *62*(3), 207-226.

Ring, U. (1994), The influence of preexisting structure on the evolution of Cenozoic Malawi Rift (East African Rift System), *Tectonics*, *13*(2), 313-326.

Ring, U., A. Kröner, R. Buchwaldt, T. Toulkeridis, and P. W. Layer (2002), Shear-zone patterns and eclogite-facies metamorphism in the Mozambique belt of northern Malawi, east-central Africa: implications for the assembly of Gondwana, *Precambrian Res.*, *116*(1), 19-56.

Ring, U., H. L. Schwartz, T. G. Bromage, and C. Sanaane (2005), Kinematic and sedimentological evolution of the Manyara Rift in northern Tanzania, East Africa, *Geol. Magazine*, *142*(04), 355-368.

Rosendahl, B. R. (1987), Architecture of continental rifts with special reference to East Africa, *Annu. Rev. Earth Planet. Sci.*, *15*, 445-503.

Rosendahl, B. R., D. J. Reynolds, P. M. Lorber, C. F. Burgess, J. McGill, D. Scott, J. J. Lambiase, and S. J. Derksen (1986), Structural expressions of rifting: lessons from Lake Tanganyika, Africa, *Geol. Soc., London, Spec. Pub.*, *25*(1), 29-43.

Salem, A., S. Williams, J. D. Fairhead, R. Smith and D. Ravat (2007), Interpretation of magnetic data using tilt-angle derivatives, *Geophysics*, *73*(1), L1–L10.

Saria, E., E. Calais, D. S. Stamps, D. Delvaux, and C. J. H. Hartnady (2014), Present-day kinematics of the East African Rift, *J. Geoph. Res.*: *Solid Earth*, *119*(4), 3584-3600.

Schlische, R. W. (1991), Half-graben basin filling models: new constraints on continental extensional basin development, *Basin Res.*, *3*(3), 123-141.

Scholz, C. A., and B. P. Finney (1994), Late Quaternary sequence stratigraphy of Lake Malawi (Nyasa), Africa, *Sedimentology*, *41*(1), 163-179.

Schrenk, F., T. G. Bromage, C. G. Betzler, U. Ring, and Y. M. Juwayeyi (1993), Oldest Homo and Pliocene biogeography of the Malawi rift, *Nature*, *365*, 833-836.

Seismological Bulletin of Malawi (2015), Malawi Geological Survey, Zomba, Malawi.

Seyitoglu, G., O. Tekeli, I. Çemen, S. Sen, and V. Isik (2002), The role of the flexural rotation/rolling hinge model in the tectonic evolution of the Alasehir graben, western Turkey, *Geol. Magazine*, *139*(01), 15-26.

Smith, R. S., and A. Salem (2005), Imaging depth, structural and susceptibility from magnetic data: The advanced source parameter imaging method, *Geophys. 70*(4), L31-L38.

Smith, R. S., J. B. Thurston, T. F. Dai, and I. N. MacLeod (1998), iSPITM—the improved source parameter imaging method, *Geoph. Prosp.*, *46*(2), 141-151.

Specht, T. D., and B. R. Rosendahl (1989), Architecture of the Lake Malawi rift, east Africa, *Jour. Afr. Ear. Sci. (and the Mid. East)*, *8*(2-4), 355-382.

Stamps, D. S., E. Calais, E. Saria, C. Hartnady, J.-M. Nocquet, C. J. Ebinger, and R. M. Fernandes (2008), A kinematic model for the East African Rift, *Geoph. Res. Lett*., *35*, L05304.

Versfelt, J., and B. Rosendahl (1989), Relationship between pre-rift structure and rift architecture in Lakes Tanganyika and Malawi, East Africa, *Nature*, 337, 354-357.

Wells, D. L. and K. J. Coppersmith (1994), New empirical relationships among magnitude, rupture length, rupture width, rupture area, and surface displacement, *Bull. Seis. Soc. Amer.*, *84*(4), 974-1002.

Wheeler, W., and J. Karson (1989), Structure and kinematics of the Livingstone Mountains border fault zone, Nyasa (Malawi) Rift, southwestern Tanzania, *J. Afric. Earth Sci. (and Mid. East)*, *8*, 393–413.

Wilson, R. W., R. E. Holdsworth, L. E. Wild, K. J. W. McCaffrey, R. W. England, J. Imber, and R. A. Strachan (2010), Basement-influenced rifting and basin development: A reappraisal of post-Caledonian faulting patterns from the North Coast Transfer Zone, Scotland, *Geol. Soc., London, Special Publications, 335*(1), 795-826.

Withjack, M. O., R. W. Schlische, and P. E. Olsen (2002), Rift-basin structure and its influence on sedimentary systems. Sedimentation in Continental Rifts, *SEPM Spec. Pub., 73*, 57–81.

Wright, T.J., C. Ebinger, J. Biggs, A. Ayele, G. Yirgu, D. Keir, and A. Stork (2006), Magma-maintained rift segmentation at continental rupture in the 2005 Afar dyking episode, *Nature*, *442*(7100), 291-294.

Zang, A., and O. Stephansson (2010), Stress Field of the Earth's Crust, *Springer*, *New York*.

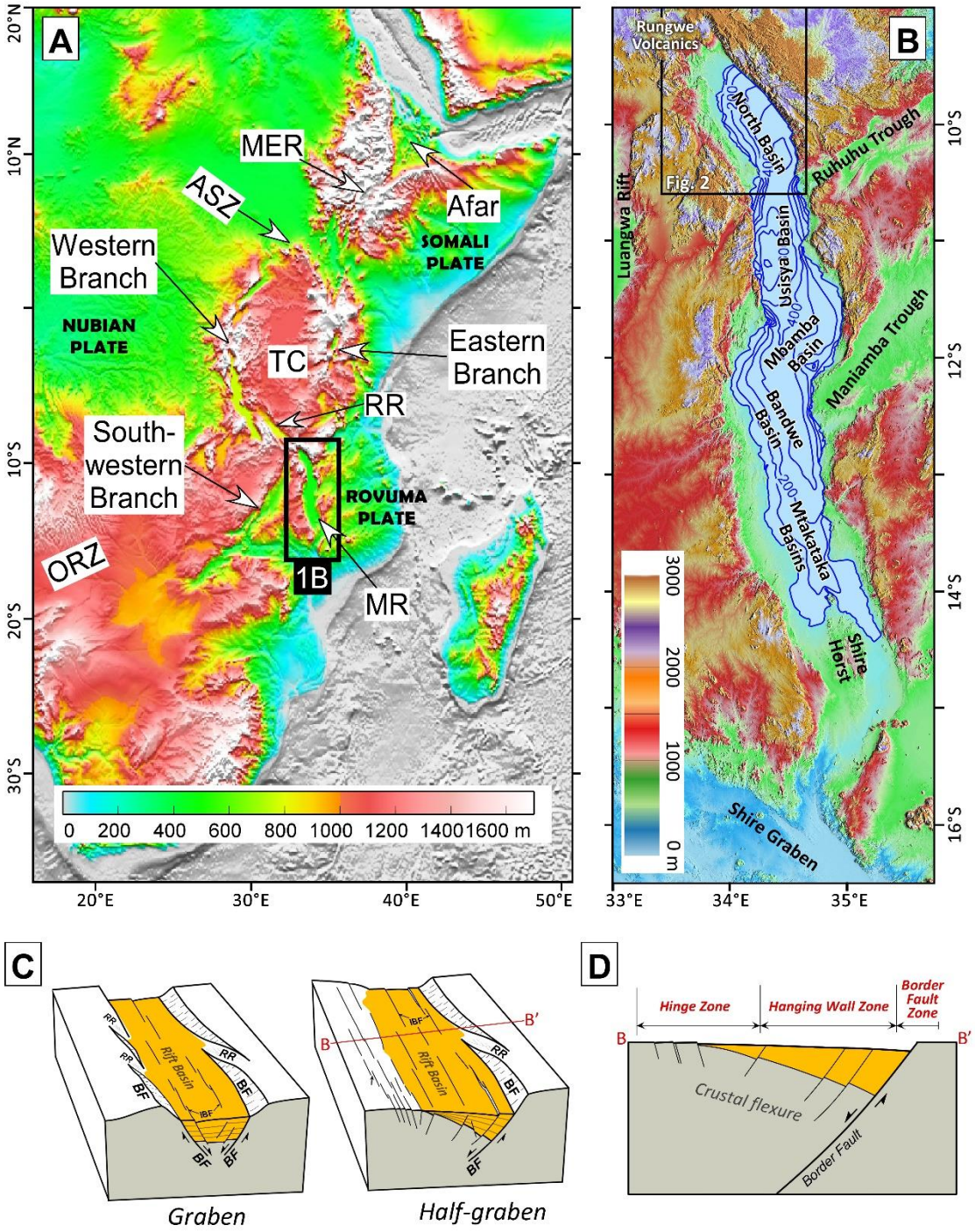

Figure 1. (a) Shuttle Radar Topography Mission (SRTM) Digital Elevation Model (DEM) of eastern Africa, showing the location of the Malawi Rift (MR) within the East African Rift System (EARS). ASZ = Aswa Shear Zone, MER = Main Ethiopian Rift, ORZ = Okavango Rift Zone, RR = Rukwa Rift, TC = Tanzania Craton. (b) SRTM DEM showing different segments of the Malawi Rift. (c) Schematic diagrams of a graben and half-graben. BF = Border fault, IBF = Intrabasin fault, RR = Relay ramp. (d) Schematic diagram of a cross-section across a half-graben, showing the overall structural architecture of a typical half-graben. For the North Basin, the Livingstone Fault represents the main border fault.

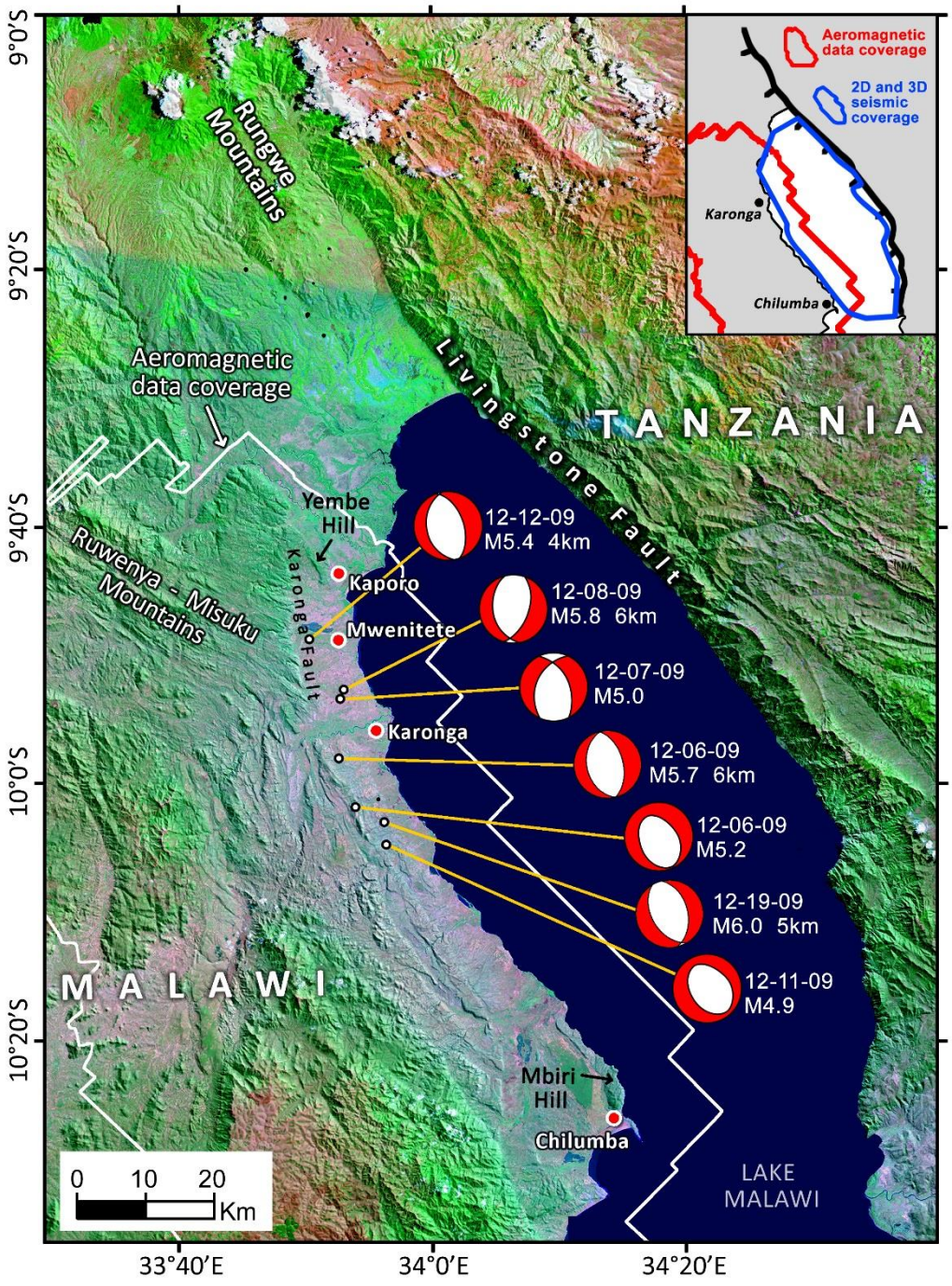

Figure 2. 742 (Red-Green-Blue) Landsat Thematic Mapper (TM) image draped onto Shuttle Radar Topography Mission (SRTM) Digital Elevation Model (DEM) of northern Malawi showing major rift-related morpho-tectonic features and location of fault plane solutions and centroid depths of $M_w \geq 4.9$ earthquakes associated with the December 2009 Karonga earthquake swarm. The earthquake data are from *Biggs et al.* [2010] and Global Centroid Moment Tensor database. White solid open polygon represents the area covered by aeromagnetic data in Figures 4 and 5. **Inset:** map of the North Basin showing the aerial coverage of previously published seismic data [blue polygon; *Mortimer et al.*, 2007] relative to aeromagnetic data coverage (red polygon; this study).

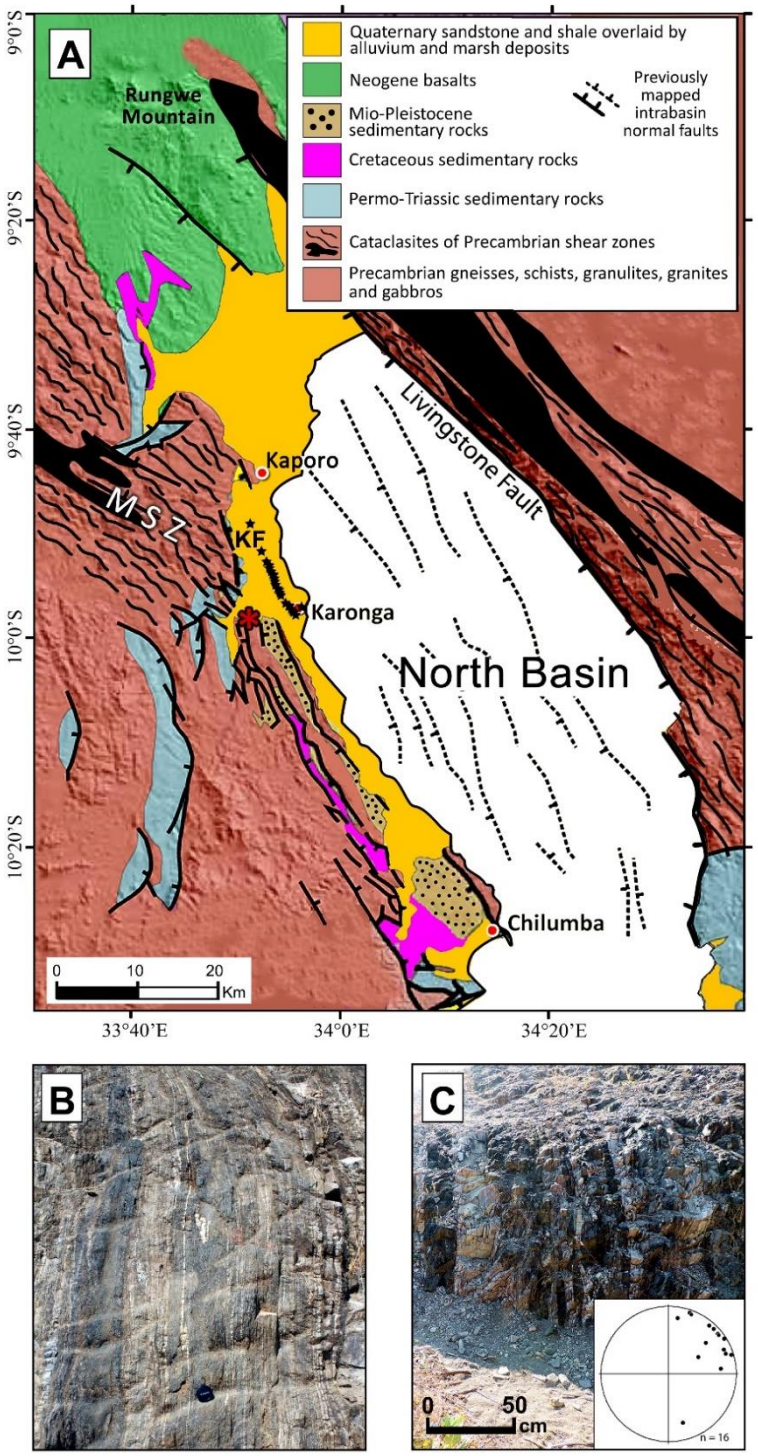

Figure 3. (a) Geological map of the North Basin of the Malawi Rift modified after *Wheeler and Karson* [1989], *Biggs et al.* [2010] and *Mortimer et al*. [2007]. MSZ = Mughese Shear Zone (Precambrian), KF = Karonga fault. (b and c**)** Field photographs of the basement fabric in the outcrops of the MSZ at a location ~10 km west of Karonga town, along M26 road (red asterisk in Figure 3a). Figure C inset is a stereonet [from *Dawson et al.*, 2017] showing orientation and steep dips of foliation and minor shear zones within the MSZ. Black stars represent locations of coseismic surface ruptures.

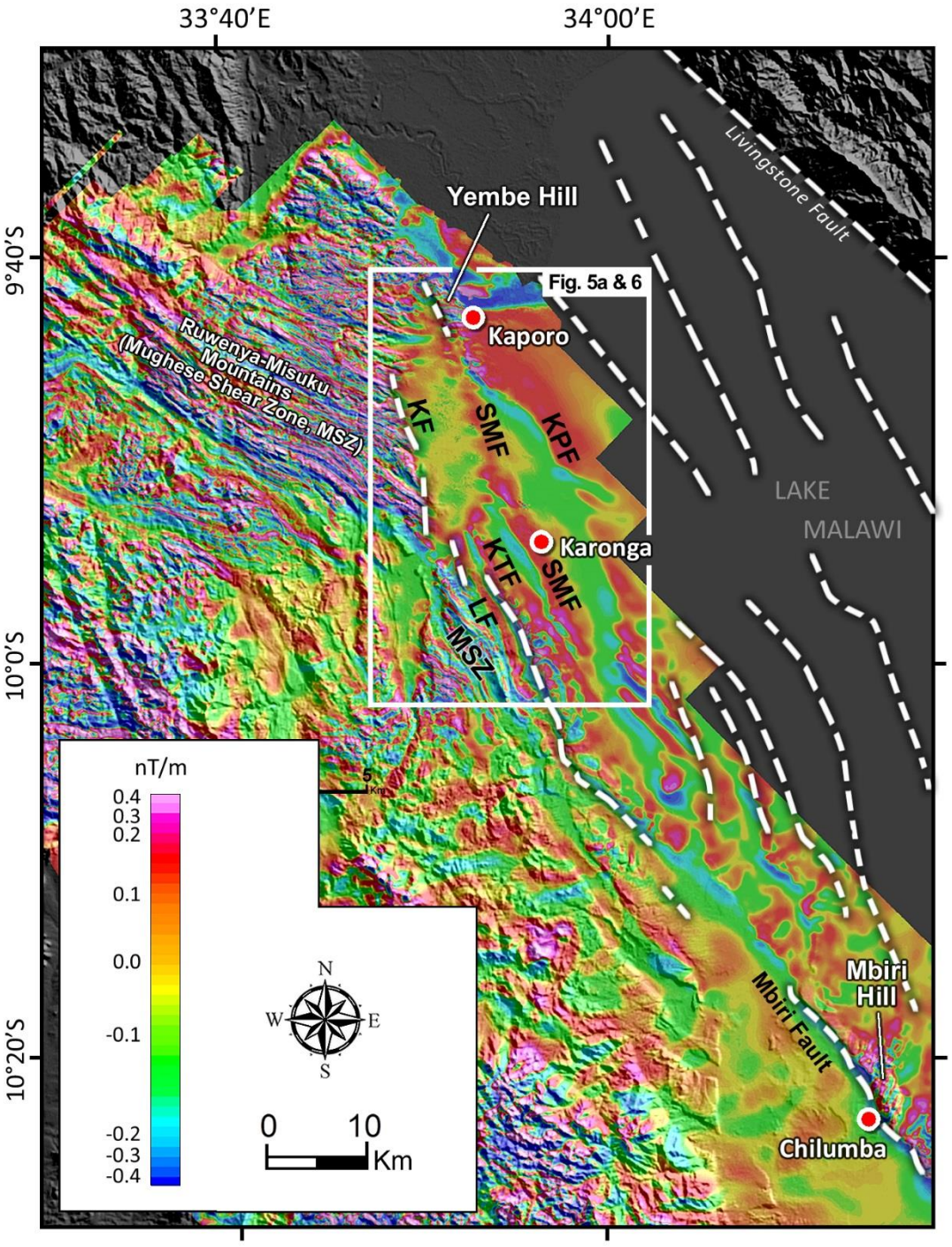

Figure 4. First vertical derivative of the RTP grid of the 2013 aeromagnetic map of Karonga-Chilumba area draped onto Shuttle Radar Topography Mission (SRTM) Digital Elevation Model (DEM), showing the relationship between surface morphology and structures in the basement. Dotted white lines represent faults interpreted from seismic data and SRTM [reported in previously published maps e.g. Figure 3a; *Mortimer et al*., 2007]. LF = Lupaso Fault, KPF = Kaporo Fault, KF = Karonga Fault, KTF = Katesula Fault, MSZ = Mughese Shear Zone, and SMF = St. Mary Fault.

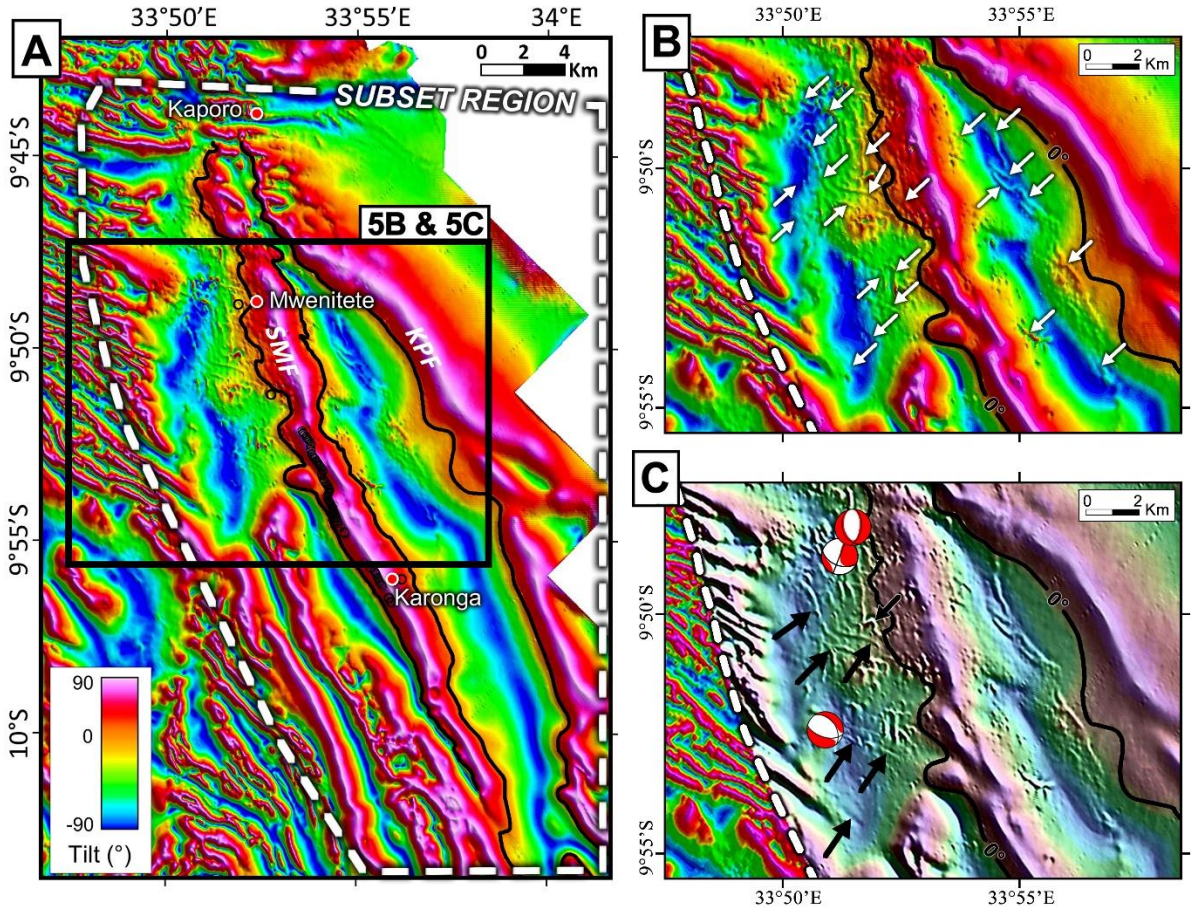

Figure 5. (a) Tilt-angle derivative of the RTP 2013 aeromagnetic TMI data. SMF = St. Mary Fault, KPF = Kaporo Fault. Black circles represent the location of surface ruptures; black solid lines represent 0° contour of the tilt-angle derivative which represents the edge of the normal faults (e.g., SMF and KPF). (b) A close-up of Figure 5a showing suppressed magnetic lineaments that are characterized by low amplitude, high frequency, short wavelength magnetic lineaments (white arrows point at some of the lineaments). (c) Tilt-angle derivative (in 5b) overlain with 45º directional gradient of the tilt-angle using transparency (area to the east of the white dotted polygon). It is not surprising that north of Karonga town, the MSZ fabric is subtly imaged in Figure 5c as the fault offsets are probably not large (Figure 9) and within magnetic basement in contrast to the more rift parallel southern segments of the SMF and KPF which have accommodated larger offset in the magnetic basement and magnetite poor sedimentary rocks (Figure 8). The earthquake fault plane solutions in Figure 5c are from *Oliva et al*. [2016].

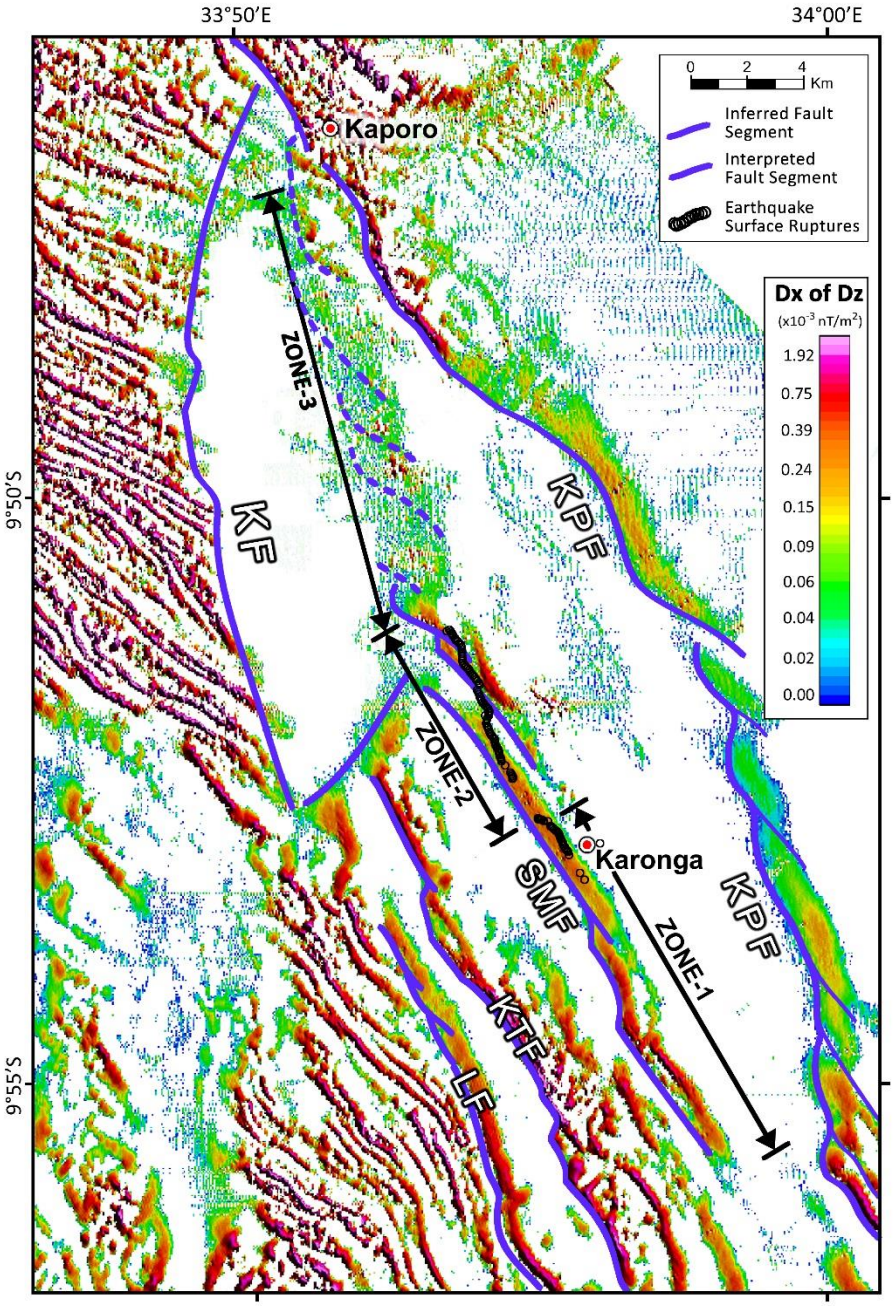

Figure 6. Horizontal-X derivative of the vertical derivative of the 2013 aeromagnetic grid covering the Karonga area showing enhanced along-strike geometry of the ruptured St. Mary Fault (SMF) and other buried faults in the area including Kaporo Fault (KPF), Katesula Fault (KTF), and Lupaso Fault (LF). Zone-1: Fault interpretation shows that the southern segment of SMF is dominated by coalesced fault segments. Zone-2: North of Karonga town, the SMF is characterized by overlapping segments separated by ~1 km-wide relay ramp. Also shown are the earthquake surface ruptures bridging this relay ramp (black circles). Zone-3: Farther north, the SMF is characterized by weakly resolved, subtle NW aeromagnetic trends (dotted lines), not corresponding to specific faults, in contrast to the southern segments where fault-related features are well resolved (solid lines). Therefore, in the poorly-resolved northern segments, we rely on fault interpretation from Dy of the vertical derivative (Figure S1b).

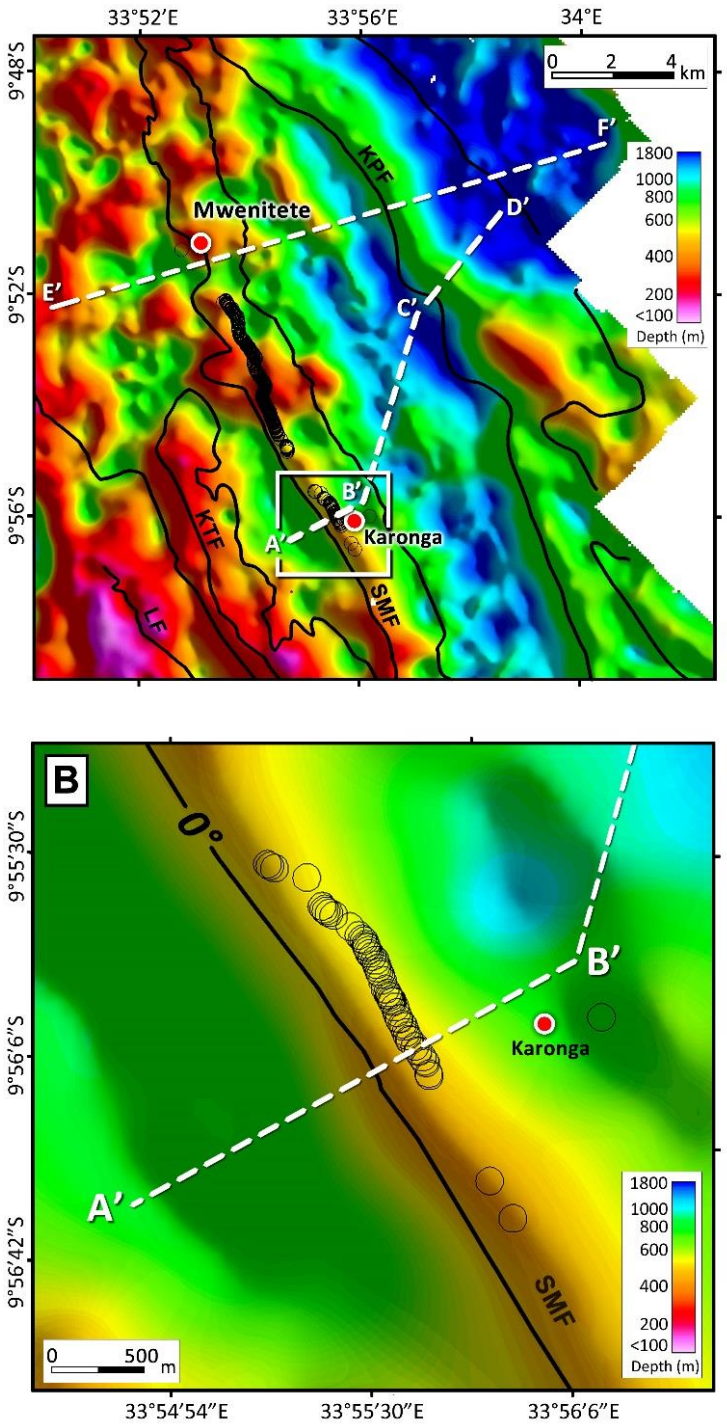

Figure 7. (a) Depth to basement map of Mwenitete – Karonga area calculated using the Source Parameter Imaging (SPI) technique, overlain with surface rupture locations (black circles). Bold contours represent the 0° tilt-angle contour (representing the edge of the basement faults). White dotted lines represent transects for cross-sections A'-B'-C'-D' and E'-F' in Figures 8 and 9. (b) Depth-to-basement map of Karonga area (area in white box in Figure 7a) showing the location of the 0° tilt-angle contour relative to the location of surface ruptures along-strike of the SMF.

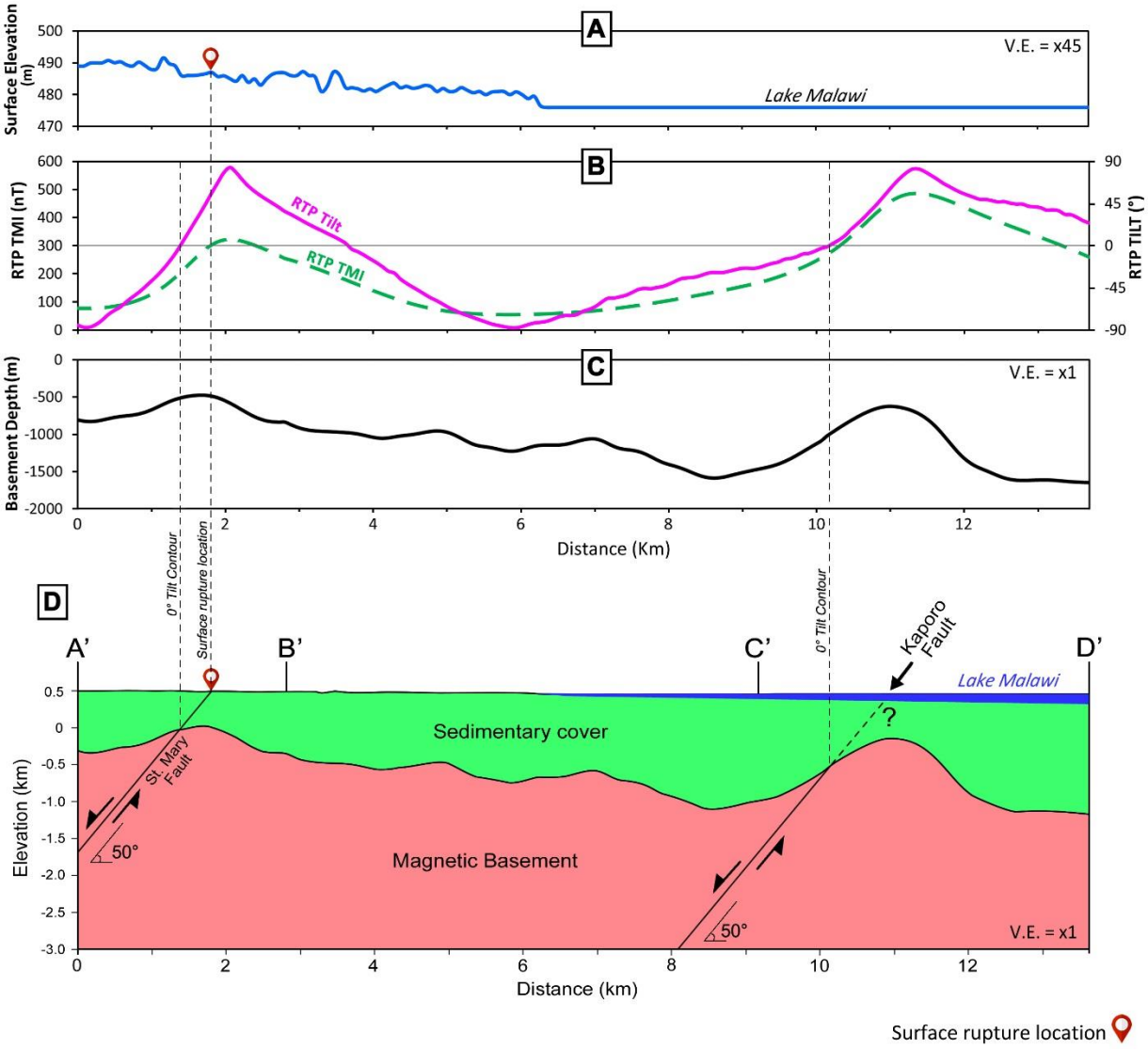

Figure 8. (a) Surface elevation, (b) Reduced-to-the-pole total magnetic intensity (RTP-TMI) and tilt-angle derivative (RTP Tilt), and (c) Depth to magnetic basement, along cross-section A'-B'-C'-D' (see Figure 7a for location). (d) Aeromagnetic geological cross-section along section A'-B'-C'-D'. We estimate a 50° dip angle for the St. Mary Fault (SMF) based on the angular relationship between the locations of the 0° tilt-angle (at basement surface) and the surface fault ruptures. Since possible coseismic surface ruptures along the Kaporo Fault (KPF) are buried beneath the lake, we infer the same dip angle as the St. Mary Fault. The selection of the 0° tilt-angle crossing on the western flanks of each of the RTP-TMI anomalies is based on independent fault dip direction from DInSAR (*Biggs et al*., 2010; *Hamiel et al.*, 2012), and geometry of the RTP-TMI gradient itself.

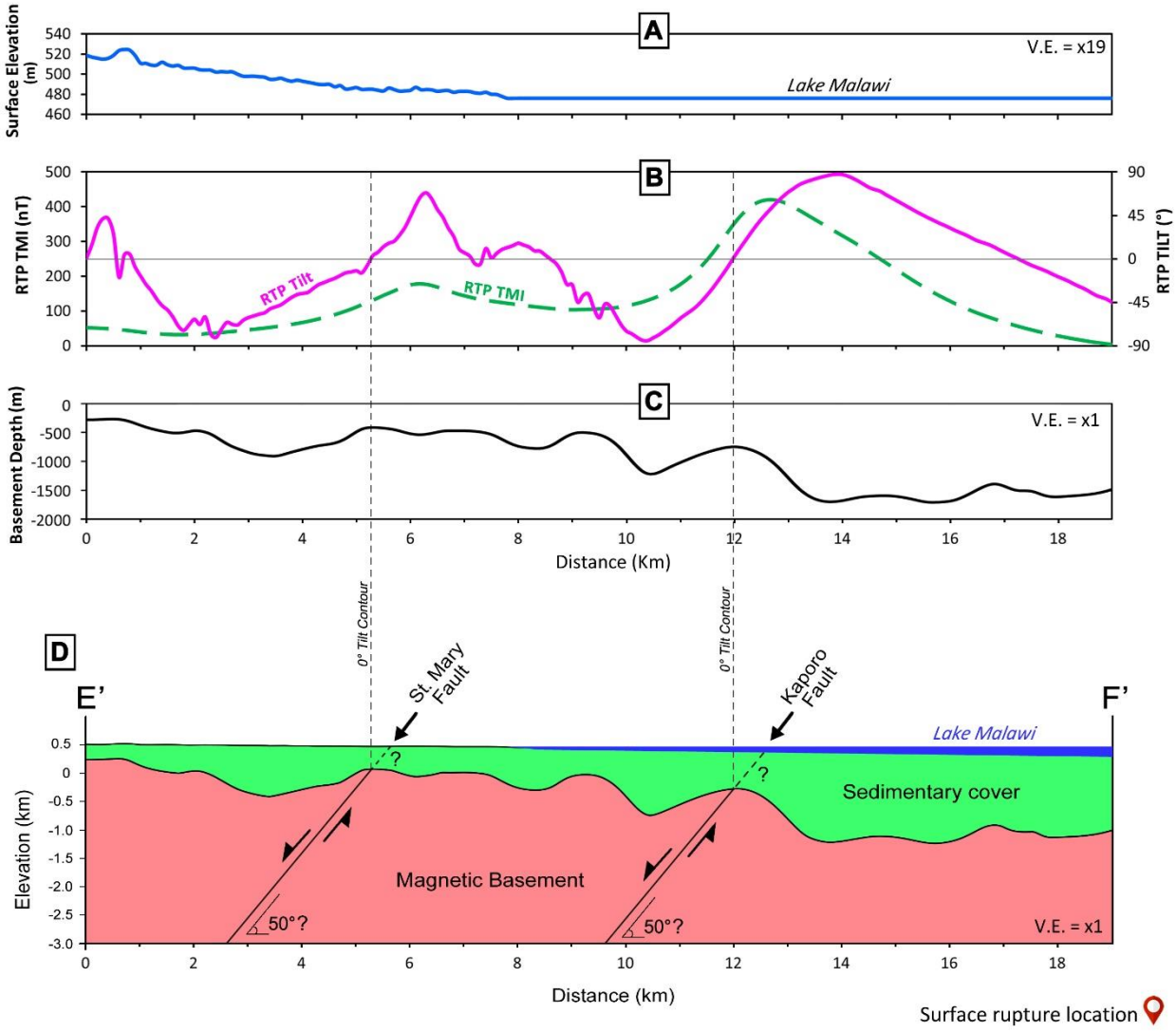

Figure 9. (a) Surface elevation, (b) Reduced-to-the-pole total magnetic intensity (RTP-TMI) and tilt-angle derivative (RTP Tilt), and (c) Depth to magnetic basement, along cross-section E'-F' (see Figure 7a for location). (d) Aeromagnetic geological cross-section along section E'-F'. We infer a 50° dip angle for the St. Mary Fault (SMF) and Kaporo Fault (KPF) based on results in Figure 8d. The selection of the 0° tilt-angle crossing on the western flanks of each of the RTP-TMI anomalies is based on independent fault dip direction from DInSAR (*Biggs et al*., 2010; *Hamiel et al.*, 2012), and geometry of the RTP-TMI gradient.

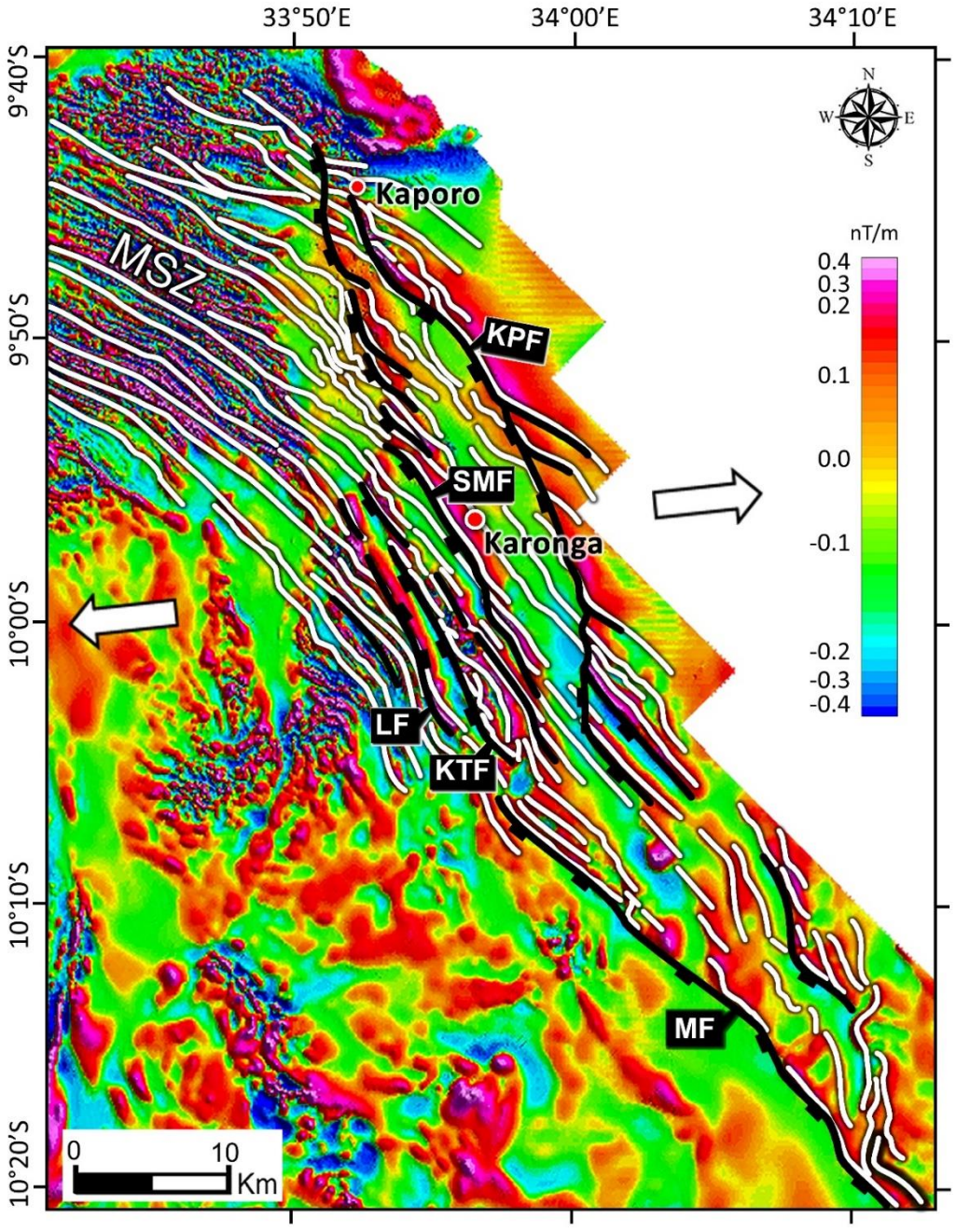

Figure 10. First vertical derivative of the 2013 aeromagnetic data of the Karonga area showing the superposition of buried normal faults (black solid lines with fault labels) on the interpreted trends of the Mughese Shear Zone (MSZ) fabric (white solid lines). White arrows indicate present-day extension direction. KPF = Kaporo Fault, KTF = Katesula Fault, LF = Lupaso Fault, SMF = St. Mary Fault and MF = Mbiri Fault.

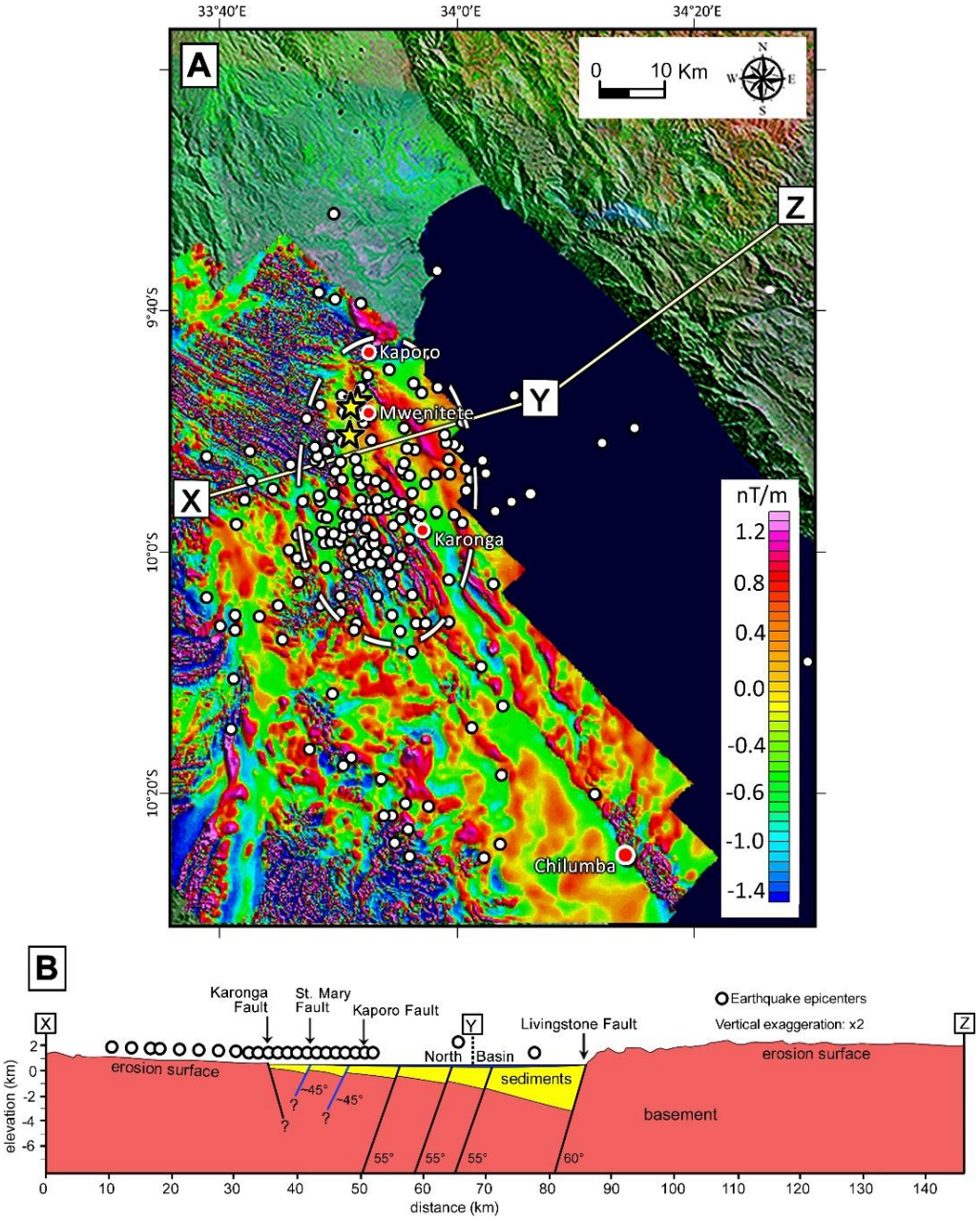

Figure 11. (a) First vertical derivative of the Reduced to Pole (RTP) aeromagnetic map of Karonga area overlaid on 742 (Red-Green-Blue) Landsat Thematic Mapper (TM) image (draped onto Digital Elevation Model) showing the location of the epicenters of earthquakes associated with the 2009 Karonga earthquake swarm (white dots). The ellipse defined by dashed white line defines the area with the greatest clustering of earthquake epicenters. Yellow stars (around Mwenitete) represent the epicenters of the M_w 5.1 2014 Karonga earthquake sequence reported by *Oliva et al*. [2016] (also shown in Figure S2b). (b) Cross-section along baseline X-Y-Z shown in Figure 11a across the North Basin [modified after *Biggs et al*; 2010], showing major faults and the projection of earthquake epicenters (white circles) to the profile line. We modify this previously published cross-section based on basement depths in Figure 9d; fault dips are from this study, *Mortimer et al.* [2007] and *Wheeler and Karson* [1989]. The projected earthquake epicenters

(associated with the 2009 Karonga earthquake swarm) cluster on the hinge zone of the North Basin half-graben.

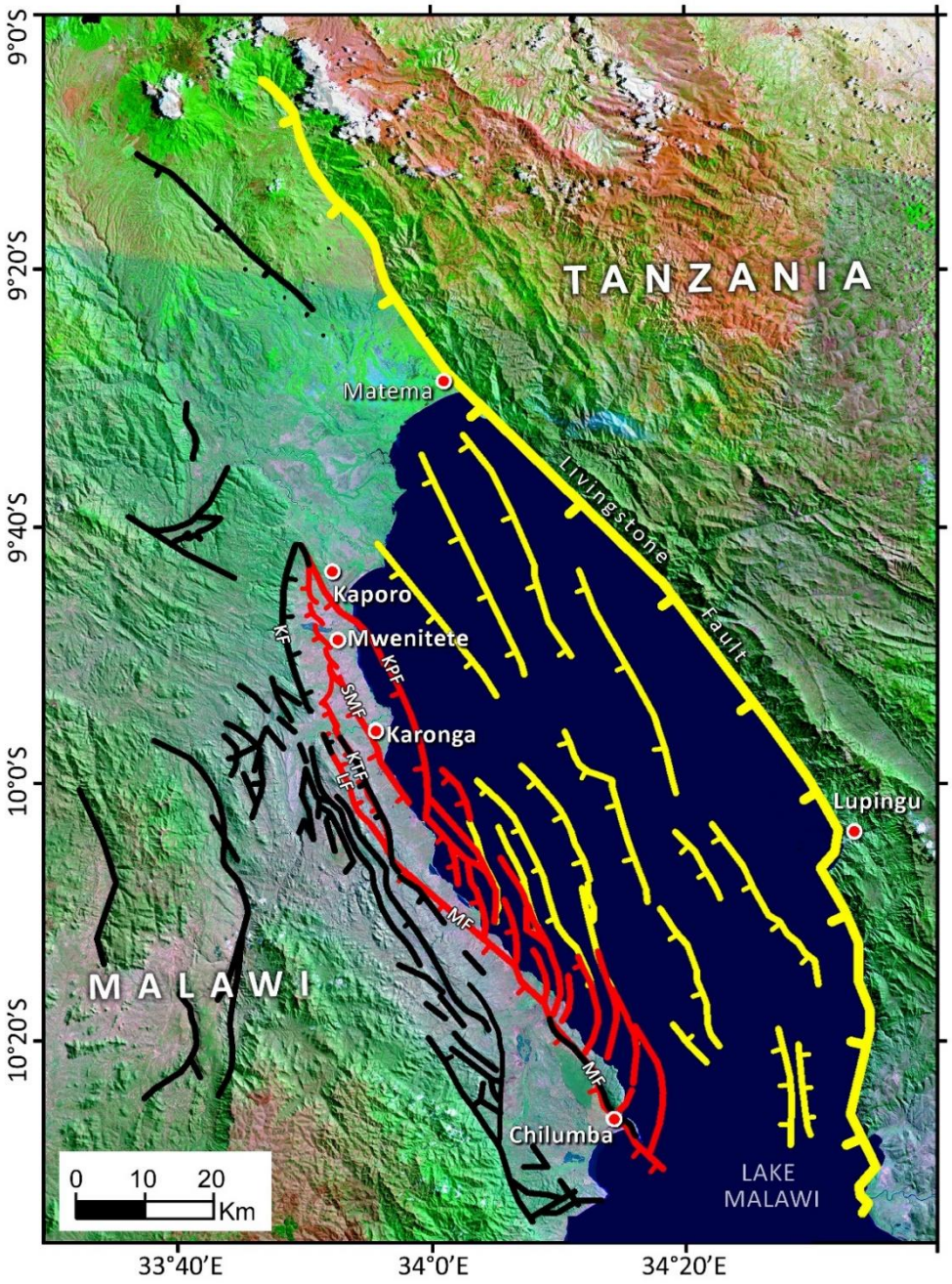

Figure 12. 742 (Red-Green-Blue) Landsat Thematic Mapper (TM) image draped onto Shuttle Radar Topography Mission (SRTM) Digital Elevation Model (DEM) of the North Basin. Red lines represent newly identified faults (from aeromagnetic data) along the hinge zone of the basin; yellow lines represent faults interpreted from seismic data [from *Mortimer et al*., 2007]; black lines represent faults observable on SRTM [reported in previously published maps e.g. Figure 3a] and aeromagnetic maps. KF = Karonga Fault, KPF = Kaporo Fault, KTF = Katesula Fault, LF = Lupaso Fault, MF = Mbiri Fault, SMF = St. Mary Fault.

[Tectonics]

Supporting Information for

[Active deformation of Malawi Rift's North Basin hinge zone modulated by reactivation of pre-existing Precambrian shear zone fabric]

[F. Kolawole[1*], E. A. Atekwana[1**], D. A. Laó-Dávila[1], M. G. Abdelsalam[1], P. R. Chindandali[2], J. Salima[2], and L. Kalindekafe[3]]

[[1]Oklahoma State University Main Campus, Stillwater, OK 74078, United States
[2]Geological Survey Department of Malawi, P.O. Box 27, Zomba, Malawi
[3]Malawi University of Science and Technology, P.O. Box 5196, Limbe, Malawi. *now at the ConocoPhillips School of Geology and Geophysics, University of Oklahoma, Norman, OK, United States
**now at the College of Earth, Ocean, and Environment, University of Delaware, Newark, DE, United States]

Contents of this file

Additional Supporting Information (Files uploaded separately)

Introduction

The supporting information below include a summary of the processing techniques applied to the aeromagnetic data covering the study area- the Karonga area of Malawi Rift's North Basin. Two aeromagnetic datasets were included in this study. The first one was acquired by Malawi Geological Survey in 1984/1985 (pre- 2009 Karonga earthquake), and the second one was acquired by the geological survey in 2013 (post- 2009 Karonga earthquake).

Text S1.

The '.kmz' files uploaded here covers the Malawi Rift North Basin and contains fault maps and filtered aeromagnetic maps. The maps presented in the .kmz files were prepared in the course of this study. We digitized the 'previously published faults' shown in Dataset 7 from *Mortimer et al.* [2007] and *Biggs et al.* [2010]. We produced the filtered aeromagnetic maps using Oasis montaj software. Before the filters were applied, the 1984/85 (Dataset S3) and 2013 (Dataset S4) total magnetic intensity data were first reduced to the magnetic pole (RTP) [*Baranov*, 1957; *Arkani-Hamed*, 1988] in order to remove the skewness of the anomalies and correctly position magnetic anomalies directly over their sources. Directional derivative filters (horizontal derivative in the x-direction (Dx), horizontal derivative in the y-direction (Dy), vertical derivative (Dz) and tilt-angle derivative) were applied to the RTP magnetic data in order to enhance magnetic gradients (edges) and highlight structural features [*Ma et al.*, 2012]. According to *Miller and Singh* [1994] and *Salem et al.* [2007], Dz, total horizontal derivative (combination of *Dx and Dy*) and the tilt-angle derivative of the RTP aeromagnetic grid enhances the magnetic signatures of shallow crustal structures.

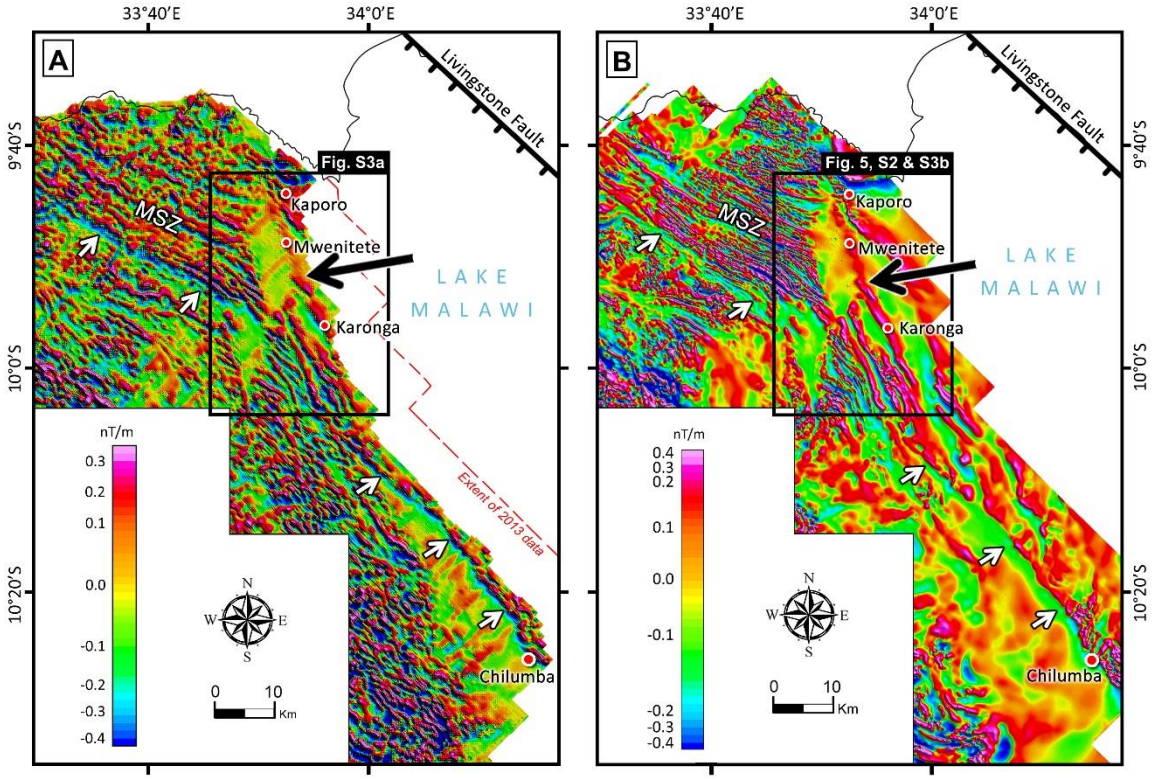

Figure S1. (a) First vertical derivative of the reduced to the pole (RTP) 1985 pre-earthquake aeromagnetic data of the Karonga area. (b) First vertical derivative of the RTP 2013 post-earthquake aeromagnetic data of Karonga area, upward continued to 120 m (same flight height as the 1985 map). Both aeromagnetic images show prominent magnetic lineament (black arrow) within the coastal plains of Lake Malawi. White arrows point to the magnetic expression of the southwestern boundary of the Mughese Shear Zone (MSZ).

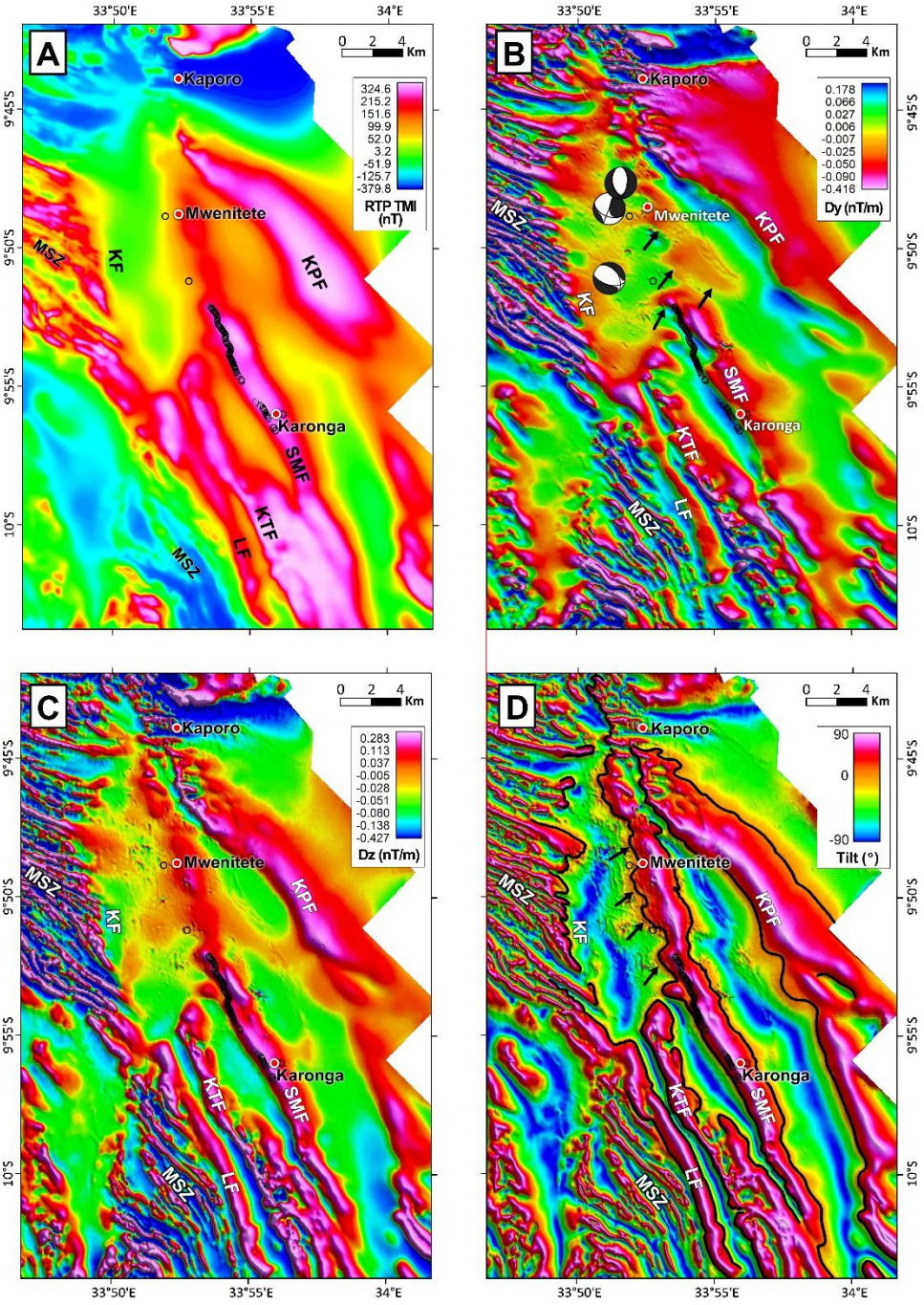

Figure S2. (a) A map of the Reduced-to-the-pole Total Magnetic Intensity (RTP-TMI) grid of Karonga area. (b) Horizontal-Y derivative (Dy) of the RTP-TMI grid. Fault plane solutions represent the December 2014 M_w 5.1 Karonga earthquake sequence [*Oliva et al.*, 2016]. Black dotted lines show orientation of en échelon segments on the northern segment of the SMF. (c) Vertical derivative (Dz) of the RTP-TMI grid. (d) Tilt-angle derivative of the RTP-TMI grid overlaid with 0° tilt-angle contour (solid black line). Black circles represent coseismic surface rupture locations. Black arrows point to orientation of en échelon segments on the northern segment of the SMF. LF = Lupaso Fault, KPF = Kaporo Fault, KF

= Karonga Fault, KTF = Katesula Fault, MSZ = Mughese Shear Zone, and SMF = St. Mary Fault.

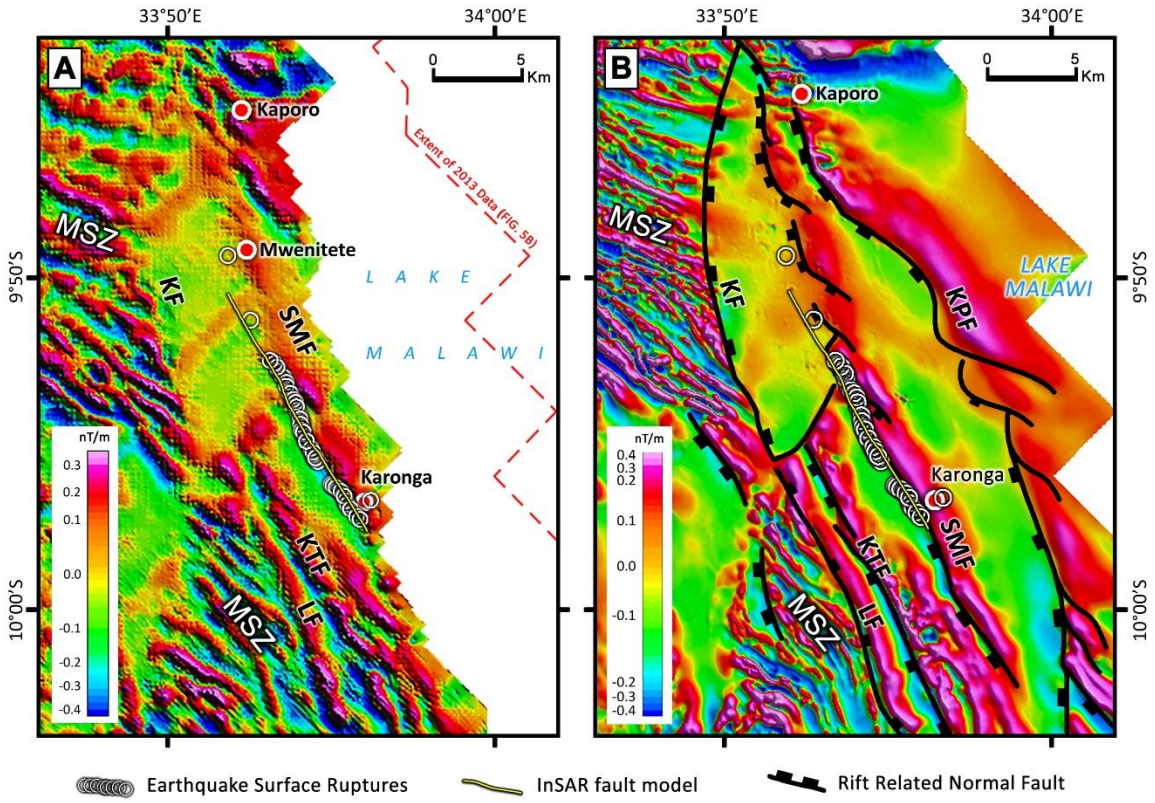

Figure S3. Correlation between the Interferometric Synthetic Aperture Radar (InSAR) fault model from *Biggs et al.* [2010] and *Hamiel et al.* [2012] (yellow line), mapped locations of the earthquake surface ruptures (white circles), and the prominent NNW- striking magnetic lineament representing the basement fabric in the Karonga area from (a) the 1984-1985 pre-earthquake, and (b) the 2013 post-earthquake aeromagnetic data (upward continued to 120 m). The two aeromagnetic maps are first vertical derivatives (Dz) of reduced to pole (RTP) grids of the two aeromagnetic grid vintages. LF = Lupaso Fault, KPF = Kaporo Fault, KF = Karonga Fault, KTF = Katesula Fault, MSZ = Mughese Shear Zone, and SMF = St. Mary Fault.

Data Set S1. .kmz file showing newly identified faults (from aeromagnetic data in this study) along the hinge zone of the Malawi Rift North Basin (black lines) and previously reported faults within the basin (e.g. Figure 3a).

Data Set S2. .kmz file showing coseismic surface ruptures for the 2009 Karonga earthquake [from Hamiel et al., 2012; Macheyeki et al., 2015].

Data Set S3. .kmz file showing first vertical derivative (Dz) of the RTP grid of the 1984/85 aeromagnetic map of the North Basin hinge zone.

Data Set S4. .kmz file showing first vertical derivative (Dz) of the RTP grid of the 2013 aeromagnetic map of the North Basin hinge zone.

Data Set S5. .kmz file showing tilt derivative of the RTP grid of the 2013 aeromagnetic map of the North Basin hinge zone.

Data Set S6. .kmz file showing contour of the tilt derivative of the RTP grid of the 2013 aeromagnetic map covering Karonga area.

Data Set S7. .kmz file showing contour of the horizontal gradient (HG) of the RTP grid of the 2013 aeromagnetic map covering Karonga area.

Data Set S8. .kmz file showing horizontal-y derivative of the tilt derivative of the RTP grid of the 2013 aeromagnetic map covering Karonga area.

Data Set S9. .kmz file showing horizontal-x derivative of the tilt derivative of the RTP grid of the 2013 aeromagnetic map covering Karonga area.

Data Set S10. .kmz file showing 45° horizontal directional gradient (HDG) of the tilt derivative of the RTP grid of the 2013 aeromagnetic map covering Karonga area.

Data Set S11. .kmz file showing depth to basement map of Karonga area calculated using the Source Parameter Imaging (SPI) technique.